The Dissertation Committee for Changbae Hyun
certifies that this is the approved version of the following dissertation:

Magnetic Studies of Colossal Magnetoresistance Materials and FePt Nanocrystals

Committee:

Alex de Lozanne, Supervisor

Brian A. Korgel

Ernst-Ludwig Florin

John T. Markert

Maxim Tsoi

Magnetic Studies of Colossal Magnetoresistance Materials and FePt Nanocrystals

by

Changbae Hyun, B.S.

DISSERTATION

Presented to the Faculty of the Graduate School of

The University of Texas at Austin

in Partial Fulfillment

of the Requirements

for the Degree of

DOCTOR OF PHILOSOPHY

THE UNIVERSITY OF TEXAS AT AUSTIN

December 2007

Dedicated to my family.

Acknowledgments

First, I would like to thank Alex for allowing me to work in his lab. During my five years in his lab, I made many mistakes, but he never blamed me. When I asked him questions about experiments or private problems, he gave me clear and reasonable advice. He created an environment that allowed me to focus on my research. He also gave me great help when I was searching for my Post Doctoral job. All my work was possible due to his advice and support.

I especially want to thank Dr. Brian Korgel and his group members, Dr. Doh Lee and Andy Heitsch. They provided me with good quality nanocrystals which allowed me to get excellent data. Without their collaboration, my PhD research time would have been much longer than five years. While searching for a PostDoc position, Dr. Korgel also recommended me, which helped me greatly in finding the position before graduation. I also want to give a special thanks to Dr. John Markert for letting me use his MFM and his SQUID magnetometer with low payment.

When I joined Alex's group, Dr. Casey Israel greeted me and gave me invaluable knowledge of Veeco Nanoscope instruments, low temperature magnetic force microscope (MFM), etc. He also guided my research and was always willing to spend time discussing data. He is smart and knows what to do intuitively. I wish him the best of luck with his research in Cambridge, England.

I also wish to thank Dr. Ayan Guha, Dr. Weida Wu, Dr. Tien-Ming Chuang, and Dr. Jeehoon Kim. When I asked questions of Ayan about instruments and basic knowledge about samples, he always taught me with a smile. Weida taught me low temperature MFM and gave me many tiny but invaluable lessons about physics. He also taught me how to do experiments with wisdom and patience. Ming was a constant lab companion for four years. He was good friend and talker. He kept our lab in a good mood and helped people. When I first had interest in Alex's lab, Jeehoon gave me good advice. He also gave me critical help when I was in trouble with the approach system for the low temperature MFM.

I also want to thank Dr. Junwei Huang. He understands physics extremely well and has priceless experience in electronics. When I had problems with electronic circuits, he would quickly diagnose what the problem was. He also has a great sense of humor, so being with him is always fun. I would like to thank my other labmates, Suenne Kim, Seongsoo Kweon, Frank Ruzicka, Alfred Lee, Morgann Berg, and Neliza León for helping with research and spending time with me. I absolutely must thank Dr. Yong Lee for his help when I was in emotional trouble. He helped me to finish my PhD research.

I received LCMO samples from Dr. G. A. Mendoza, Dr. M. E. Gomez, and Dr. J. G. Ramirez. With their help, I was able to measure the samples with the low temperature MFM and add the results to my dissertation.

The machine shop staff was a great help to me. I was able to accelerate my studies with the help of Jack Clifford and Allan Schroeder. It was nice having the freedom to machine what I designed by myself. The time spent in the machine shop was beneficial and the experience with them will form a solid base for my future research.

At last, I would like to thank my parents, my brothers, and my sisters. They were always with me and supported me all the way.

Magnetic Studies of Colossal Magnetoresistance Materials and FePt Nanocrystals

Publication No. ________________

Changbae Hyun, Ph.D.
The University of Texas at Austin, 2007

Supervisor: Alex de Lozanne

This dissertation introduces scanning probe microscopy (SPM) and describes the construction and design of a home built low temperature magnetic force microscope (MFM). Then the magnetic coatings on atomic force microscope cantilevers with a focused ion beam (FIB) will be explained. This technique allows the convenient deposition of complex or expensive materials such as CoCrPt. With the MFM tip coated by FIB, the ferromagnetic domain structure of a $La_{0.67}Ca_{0.33}MnO_3$ film is studied as a function of an in-plane magnetic field below room temperature. Next I will discuss the use of chemically-synthesized FePt nanocrystals as a good candidate for high density storage media. This nanocrystal film showed sintering problems during the annealing process, which is essential to make FePt a hard ferromagnet. A silica overcoating method was used to prevent nanocrystal sintering, which allowed the MFM study of films made from these nanocrystals. I will also discuss resistance measurements of the FePt nanocrystals.

Table of Contents

List of Figures

Chapter 1

Introduction to Scanning Probe Microscopy

Scanning probe microscopy (SPM) is a technique that studies the surface structure of specimen using a probe. The specimen or the probe is moved in a raster scan, line by line, while the probe-surface interaction is recorded as a function of position. Scanning tunneling microscopy (STM) was invented by Binnig et. al. in 1982 [1] as the first type of SPM. In STM, the probe is sharp metallic tip and the tunneling current between the tip and a metallic sample is measured. After the introduction of the STM, many scanning probe microscopes were developed to detect van der Waals force [2], magnetic force [3], electrostatic force [4], etc. between tip and surface.

1.1 Atomic Force Microscopy

MFM is based on another SPM, namely the atomic force microscope (AFM). In AFM, a tip measures van der Waals forces from a sample. The tip is attached at the end of a cantilever with a spring constant c_L. When the tip detects a force, F from a sample, the cantilever will deflect by the amount of F/c_L. The deflection of a cantilever is measured by a delicate sensor and is used for acquiring topography of a sample. There are many modes of measuring topography of a sample in AFM.

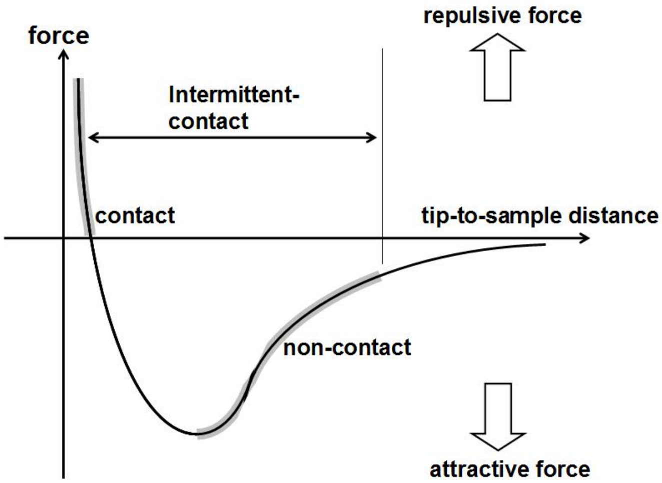

Figure 1.1: Van der Waals force and AFM Scanning modes.

The simplest way to get the topography of a sample is Contact mode. In this mode, a tip will be located in the repulsive force region as shown in Fig. 1.1. The amount of deflection of a cantilever is proportional to the repulsive force. The tip sample distance and the repulsive force are maintained at a constant vlaue by feedback control, adjusting the deflection of a cantilever to a fixed value. So a small area of raster scan with feedback control will produce the topography of a specimen. In vacuum or atmosphere, the sample is covered by an adsorbed gas layer mostly formed from water vapor. When a tip is close to sample, the meniscus spans and connects tip and surface, resulting in attractive meniscus force. Some sample may trap electrostatic charge contributing to additional substantial attractive forces between tip and surface. All these forces combine and define a minimum normal force. As the tip scans over the surface, a frictional force arises due to this minimum normal force. The frictional force causes tip damage and topographic data distortion.

The non-contact mode was developed to overcome the problem induced from the frictional force and the meniscus force. In this mode a tip scans in the attractive van der Waals forces region. Since the attractive van der Waals forces are weaker than the forces in Contact mode, a lock-in technique is used to detect such small forces. A tip is oscillated and then the change in oscillation amplitude, phase or frequency is measured for feedback control to get topography. To achieve higher resolution, the tip is located in the van der Waals force gradient region ($5 \sim 15$ nm), as shown in Fig. 1.1. In atmosphere, the meniscus layer is generally thicker than the region of the van der Waals force gradient so that the imaging with non-contact mode is seldom possible. In UHV this method is useful since the contaminant layer is thin or nonexistant.

Tapping mode is mostly used to acquire topography in AFM. In this mode the tip is oscillated with a larger amplitude than the Non-contact mode, usually greater than 20nm, so that it taps the surface. This mode is also called as Intermittent Contact Mode (Fig. 1.1). The cantilever oscillation amplitude is maintained at a fixed value by a feedback control. The amplitude of the cantilever's oscillation is large enough to overcome the tip-sample adhesion force. This also prevents the tip from sticking to the surface and causing sample damage. Since the tip oscillates vertically, frictional force does not cause a problem in Tapping mode. As shown in Fig. 1.1, the operating range is large and linear so the feedback system is stable.

1.2 Magnetic Force Microscopy

MFM was first demonstrated by Martin et al.[3] by imaging magnetic fields using a magnetized tip with 100nm resolution. In MFM, the tip is coated with magnetic material to sense a stray magnetic field from the surface. Magnetic interactions are weak but long-range compared to van der Waals forces, so that the magnetic interaction is dominant above tens of nanometers in tip-sample height. In MFM a two-pass method is used to minimize of the influence of topography. In the first pass the topography is obtained by Contact or Tapping mode. In the second pass the tip is lifted to a selected distance and the distance between tip and the obtained topography is maintained constant. MFM image is taken in the second pass scan. The magnetic interaction energy between the tip and sample is

$$U = -\int_{tip} \mathbf{M_{tip}}(\mathbf{r}) \cdot \mathbf{B}(\mathbf{r}) dr \tag{1.1}$$

where M_{tip}(r) is magnetic moment of the tip, and B(r) is the stray field from the sample. Many simulations of M_{tip}(r) have been published to calculate MFM images quantitatively.[5] [6] [7] But dipole magnetic moment approximation is simple and applicable in most case as described in appendix B. With this approximation, The MFM tip moment is considered as a point dipole moment m$_{eff}$ with only z component. So the Eqn. 1.1 can be simplified as

$$U = -\mathbf{m_{eff}} \cdot \mathbf{B} = -m_z \cdot B_z \tag{1.2}$$

Therefore magnetic force is

$$F = -\Delta U = \frac{\partial B_z}{\partial z}\hat{z} \tag{1.3}$$

In these days the magnetic force (gradient) can be detected assuming a harmonic oscillator model. The cantilever is driven near its resonant frequency. When the cantilever feels a force gradient (∂F/∂z), the effective spring constant (c$_{eff}$) changes as following approximation:

$$\begin{aligned} F &= -c_{eff} z \approx -c_L z + \frac{\partial B_z}{\partial z} z \\ c_{eff} &= c_L - \frac{\partial B_z}{\partial z} \end{aligned} \tag{1.4}$$

An attractive force gradient softens the cantilever while a repulsive force gradient makes the cantilever stiffer. From the simple harmonic oscillator model, the new resonant frequency will be

$$f = \frac{1}{2\pi}\sqrt{\frac{c_{eff}}{m_{eff}}} = \frac{1}{2\pi}\sqrt{\frac{1}{m_{eff}}\left(c_L - \frac{\partial f}{\partial z}\right)} = f_0\sqrt{1 - \frac{1}{c_L}\frac{\partial f}{\partial z}} \tag{1.5}$$

Since the ∂F/∂z ($10^{-6} \sim 10^{-3}$ N/m) is usually smaller than c_L ($0.1 \sim 5$ N/m), using Taylor expansion, the equation becomes:

$$\Delta f = f - f_0 = -\frac{f_0}{2c_L}\frac{\partial F}{\partial z} \tag{1.6}$$

To detect the frequency shift, “slope detection” [8] and frequency modulation (FM) techniques are used. In slope detection the time constant (t) is $2Q/\omega_0$. In high vacuum, the time constant is around 0.1 second, so we can not use the slope detection method. But FM technique is not affected by the quality factor (Q). In FM technique, the minimum detectable force gradient is given by [9]

$$\Delta F'_{min} = \sqrt{\frac{4k_B c_L T B}{2\pi f_0 Q A^2}} \tag{1.7}$$

where $F' = \partial F/\partial z$, k_B is Boltzmann's constant, T is temperature, c_L is the spring constant of the cantilever, B is the measurement bandwidth, and A is the oscillation amplitude. Therefore the sensitivity will increase in high vacuum.

Chapter 2

Design of Low temperature MFM

While few low temperature MFMs have been developed in laboratories around world,[10] [11] [12] Our group has been the most active in the development and application of this technique. We use two types of cantilever detection techniques in low temperature MFMs: piezoresistive detecting sensor[13] and optical interferometer[14]. In this chapter, a LT-MFM that utilizes a piezoresistive cantilever will be described. This LT-MFM was designed by Alex de Lozanne.

2.1 Cantilever

Piezoresistive cantilevers (piezolevers) incorporate a doped Si layer that undergoes resistance changes proportional to lever deflection changes.[15] This resistive layer serves as one arm of a dc–biased Wheatstone bridge that converts the resistance into a voltage signal (see Fig. 2.1).[16] This provides a simple way to read out lever deflection without the added complication of optical alignment and thermal drift issues that can accompany optical detection methods like fiber–optic interferometry. The disadvantages of choosing a piezoresistive deflection sensor are possible sample heating effects due to

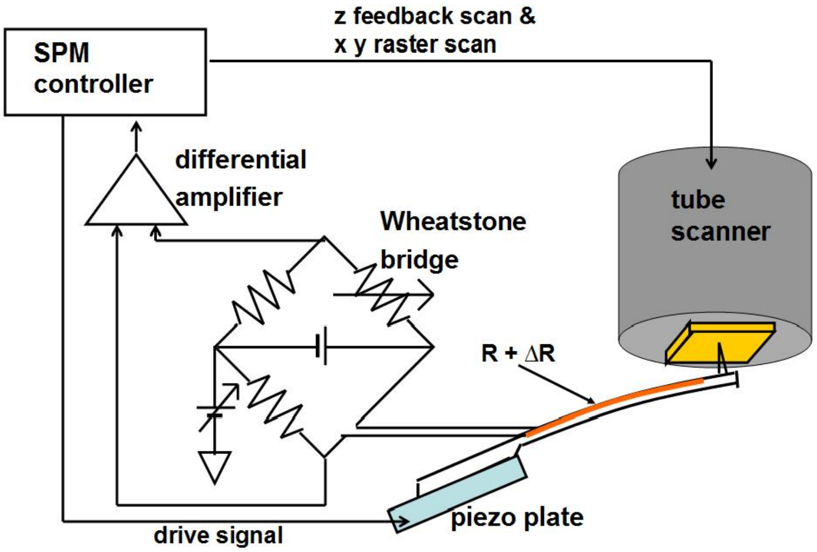

Figure 2.1: MFM diagram using piezoresistive cantilever.

the power dissipated in the lever and dealing with noise levels elevated above the noise limit set by thermal excitation of the cantilever (empirically seen by Volodin et al. [12] and our group). We chose to use piezolevers over an optical detection scheme because many of the material systems we study have magnetic transitions that span wide ranges of temperatures. If we want to track an area of the sample while varying the sample temperature from 250 K to 5 K and back, we can eliminate any possible optical misalignment induced by thermal drift by using piezolevers. Because the material systems of interest have relatively high magnetization values, the noise increase is rendered inconsequential. Sample heating may be an issue at the lowest temperatures, where heat capacities are lowest. We limit sample heating by placing an upper bound of 2 K on allowable cantilever heating through considerations of heat exchange gas pressures, heat conduction pathways, and piezolever power dissipation using the reasoning outlined by Giessibl et al. [16]

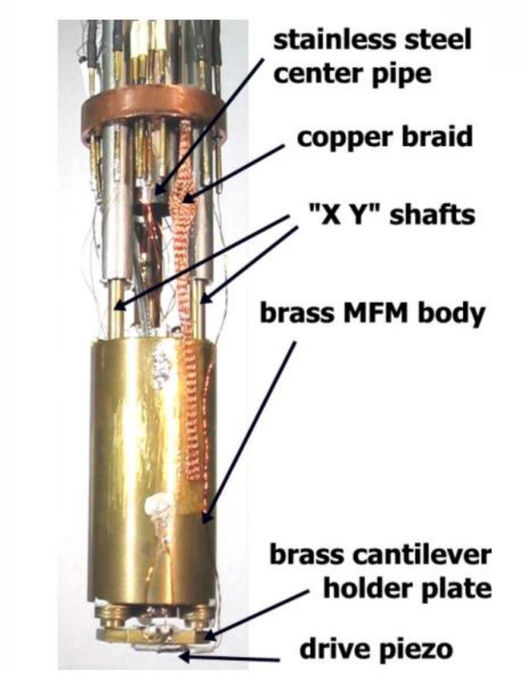

Figure 2.2: Details of the MFM probe.

Our first piezolevers were made by M. Tortonese at Park Scientific Instruments. Recently we found a manufacturer of piezolevers in Japan (Seiko Instruments) with a distributor in the USA (KLA–Tencor). We have used both PRC400 and PRC120 cantilevers with spring constants of 2–4 N/m and 30–40 N/m, respectively. Since piezolevers are not currently available with a magnetic coating, we deposit Fe, Co, $Co_{85}Cr_{15}$, or $Co_{71}Cr_{17}Pt_{12}$ on the lever and integrated tip by evaporation or by sputtering, taking care to avoid shorting the piezoresistor embedded in the lever. The detail of $Co_{71}Cr_{17}Pt_{12}$ coating will be described in chapter 3. The cantilever chip is fixed, tip pointing upward, to a brass cantilever holder plate with silver paint or epoxy. This plate is held against the bottom of the instrument, as shown in Fig. 2.2, has a hole cut in the center for optical access to the tip/sample region, and is thermally linked to the brass MFM body with a copper wire (0.32 mm diameter). A driving piezo plate is attached to the cantilever holder plate and serves to excite the resonance of the cantilever.

2.2 Scanner

We use the same tube scanner as in the previous design, a PZT–5H tube with four external electrodes and one internal electrode, 51 mm long, with outer diameter (OD) of 6.35 mm and wall thickness of 0.51 mm (Staveley Sensors). The maximum range of this scanner (±200 V applied to outer electrodes) is approximately 160 μm at 293 K. The scan tube fits inside a hole in the cylindrical brass MFM body and is fixed at the top with a Macor adapter (Fig. 2.2). The sample is mounted with the surface facing down on a copper sample stage attached to the bottom of the scan tube just past the end of the MFM body. A Cernox temperature sensor (LakeShore) and a heater resistor are mounted on opposite sides of the sample stage. The copper sample stage is thermally linked to the MFM body with a copper wire (0.16 mm diameter). The MFM has four leads that can be used to connect to the sample to measure bulk resistivity or resistance of a patterned device in situ as a function of temperature and applied magnetic field.

2.3 Positioner

The x–y–z positioner is based on the traditional kinematic three–point mount: one ball fits into a cone on the cantilever holder plate, the second ball fits into a V–shaped groove, and the third ball presses against a flat surface. We chose sapphire for the balls and the flat surface due to its high rigidity and low friction with the aim of reliable, nonhysteretic motion. The third ball is driven by a 10–80 screw, which provides a very smooth approach mechanism in the $\hat{z}$ direction. The 10–80 screw is driven by a dedicated rotary manipulator at the top of the probe, coupled by a thin stainless steel pipe.

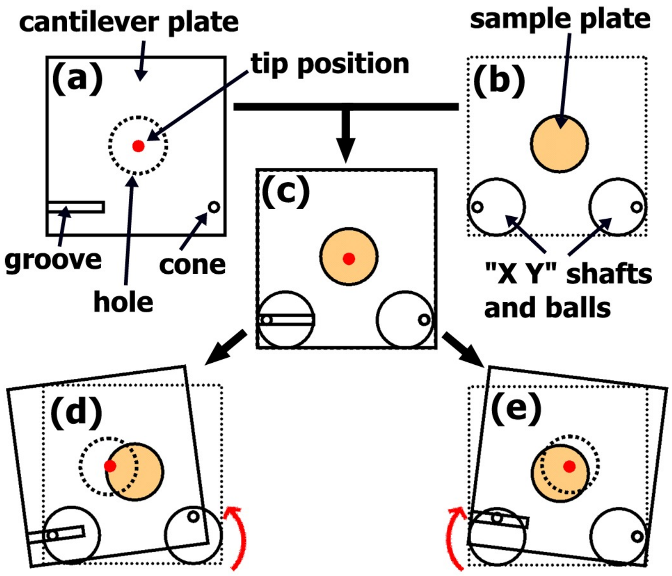

Figure 2.3: Schematic (looking along the probe axis from below) of (a) cantilever holder plate and lateral offset mechanism relative to (b) sample plate. (c) Cantilever plate superimposed on sample plate and "x–y" shafts and balls. (d) Cantilever plate offset after 90° rotation of rightmost shaft in (c). (e) Cantilever plate offset after 90° rotation of leftmost shaft in (c).

The novel aspect of this design is that it provides quasi–x–y positioning in a very compact design by mounting the first two balls mentioned above in an off–center position on rotating shafts, as shown in Fig. 2.3. When the first shaft is rotated, the first ball, which fits into a cone on the cantilever holder plate, makes this cone rotate in a circle about this shaft while the second ball slides along the V–shaped groove, as depicted by Fig. 2.3(c,d). For small rotations, this makes the tip of the cantilever travel in an arc over the sample. When the second shaft is rotated, as in Fig. 2.3(c,e), the second ball slides inside the V–shaped groove, causing the cantilever holder plate to pivot about the first ball. The balls are offset by 0.76 mm from the center of the shafts, providing a maximum travel of 1.5 mm. However, the maximum range extends into a highly nonlinear regime, so the practical range is limited to several hundred microns. When the shafts for "x" and "y" are positioned as in Fig. 2.3(d), the quasi–linear portion of the motion is also quasi–orthogonal. We use quotes for "x" and "y" to emphasize the fact that these two axes are neither linear nor orthogonal over long distances.

The shafts for "x" and "y" are rotated by thin stainless steel pipes that extend up to the top of the probe, where the head of a socket head screw is mounted on each pipe. The details of how these pipes couple to the rotating shafts on the MFM body are discussed in the next section. A single rotary manipulator attached to the top of the probe with a bellows drives a ball–head Allen key to engage and rotate either the "x" or "y" motion. Having separate, dedicated rotary manipulators for "x" and "y" would be more convenient although it would add to the cost and weight of the probe.

2.4 Support

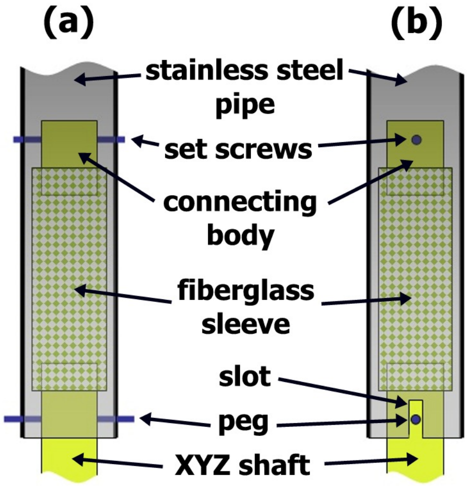

Figure 2.4: Peg and slot rotational coupling from an x–y–z pipe to an x–y–z shaft. (a) is rotated 90° with respect to (b).

The MFM body is supported by the equilateral arrangement of the three thin pipes (6.35 mm OD, 0.15 mm wall, stainless steel) that provide rotary motion for x, y, and z positioning. To reduce vibrational coupling, the weight of the MFM body is supported by a short piece of fiberglass sleeve material on each shaft, while the torque is transmitted using a “peg and slot” arrangement, as shown in Figure 2.4. The three thin pipes are held in place, but allowed to rotate, by a copper heat sink above the MFM body and a similar aluminum circular plate at the top of the probe. The copper heatsink and aluminum plate are connected by a thin central pipe (11.1 mm OD, 0.15

mm wall, stainless steel) that provides rigidity for the probe as a whole. The aluminum plate at the top of the probe is free to slide up and down to accommodate differential thermal contraction, and the weight of the whole probe (or optional springs) provide the necessary force to press the copper heatsink against a copper sheath at the bottom of the pipe housing (described in the following section).

2.5 Chamber

The top of the probe has a small chamber made from a standard four–way cross with 70 mm flanges. The top flange connects to the two rotary manipulators mentioned above, while one side flange has a 20 pin feedthrough for electrical leads and the other side flange connects to a valve and pumping system. The bottom flange connects to the pipe housing for the instrument. The pipe housing is a standard stainless steel tube (31.8 mm OD, 0.71 mm wall). The pipe housing is removed every time a tip or sample is replaced. While this is not as convenient as having a small canister attached at the bottom, it has the reliability and long life of a seal that remains at room temperature at the top of the probe.

In order to improve the thermal conductivity to the bath, the bottom of the pipe housing was machined to remove 0.33 mm from the inner wall, and a copper sheath (31.0 mm OD, 0.76 mm wall, 101 mm long) was press–fit into it. The copper heatsink presses against the top of this copper sheath and is thermally linked to the MFM body with a copper braid for better heat transfer from the MFM to the bath.

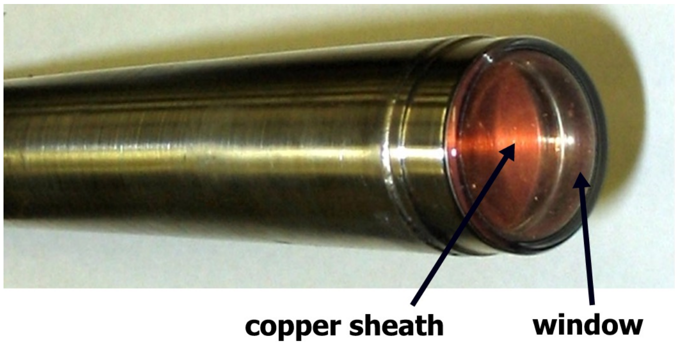

Figure 2.5: MFM pipe with integrated window. The copper sheath is visible behind the window.

The window at the bottom of the pipe housing (see Fig. 2.5) is an important feature of this design. We started with a standard glass viewport mounted on a standard NW25 flange (Model KVP–100 from MDC vacuum). The tapered portion of the NW25 flange was carefully machined away in order to match the 31.8 mm OD of the pipe housing and a short instep was machined for alignment purposes. It was then welded at the bottom of the pipe housing. The differential thermal contraction between the glass window and the stainless steel body is taken up by a thin Kovar sleeve. Nevertheless, approximately half a year of thermal cyclings produced a small crack that started on one side of the glass window and propagated to the opposite side over approximately one more year. Surprisingly, the crack did not produce a measurable leak until it crossed the complete window, but fortunately it was possible to seal it with varnish (Kurt J. Lesker KL–5 leak sealant). We believe that this crack was initially due to a manufacturing defect, or some shock during machining or handling. An identical pipe and window has been thermally cycled from 77 K to room temperature roughly 100 times with no cracks thus far.

2.6 Electronics

We drive the scanner and acquire imaging data with a Nanoscope IIIa controller (Veeco–Digital Instruments). The lever deflection signal from the Wheatstone bridge is differentially amplified by a Stanford Research Systems SRS 560 Preamplifier (see Fig. 2.1). For MFM operation we use the frequency modulation technique [9], both with the commercial "Extender" available for the Nanoscope controller or with a digital phase lock loop (EasyPLL from Nanosurf). The latter required homemade electronics to interface with the Nanoscope controller. The homemade electronics consist mainly of a phase shifter to choose the phase setpoint for the phase lock loop and an rms–to–dc converter and comparator to generate the feedback signal for amplitude modulated scans. Albrecht et al. showed that the minimum detectable force gradient using the frequency modulation technique is

$$\delta F'_{\mathrm{min}} = \sqrt{\frac{4\,k\,k_B\,T\,B}{w_0\,Q\,A^2}}\,, \tag{2.1}$$

where $w_0/(2\pi) = f_0$, Q is the quality factor of the lever, k_B is Boltzmann's constant, T is the temperature, and B is the measurement bandwidth. [9]

We operate the MFM in one of two modes, depending on the surface roughness of the sample. For flatter samples we generally use constant–plane scanning, recording the resonant frequency shift of the cantilever while scanning a plane aligned to and lifted off the sample surface. For rougher samples this scanning mode would result in a large average tip/sample distance and large variations in the tip/sample distance. Therefore, for rougher samples we generally use an interleaved scan mode, lift mode, whereby one line of topography (AFM) is acquired in frequency–modulated tapping mode (constant amplitude scanning) and then one line of MFM data is acquired by retracing the same topography at a certain lift height above the sample (while recording the resonant frequency shift of the cantilever). The interleaving of the topographic and magnetic images assures that they are spatially correlated, even when thermal drift is present. To null any electrostatic interaction between the tip and sample, the tip potential can be adjusted by changing the potential of the whole Wheatstone bridge.

Chapter 3

MFM Tip Coating with Focused Ion Beam

Focused ion beams (FIB) are becoming increasingly essential as tools in the fabrication and characterization of nanostructures, typically used to remove material from a narrow selected area.[17] [18] Though less common, material can also be deposited directly from the beam or by localized decomposition of precursor gases.[17] [18] Yet another application of FIB is to expose resist in order to generate patterns.[19] Here we demonstrate that material can be deposited over a small area of interest by sputtering a nearby target with the focused ion beam. In our particular application we deposit a magnetic thin film on the tip of an atomic force microscope (AFM) cantilever,[1] thereby sensitizing the lever to magnetic forces and creating a magnetic force microscopy (MFM) cantilever.[3]

3.1 Motivation

Our interest in developing this technique is threefold. First, it allows us to deposit expensive materials, such as $Co_{71}Cr_{17}Pt_{12}$,[20] without needing to buy a relatively large sputtering target. Second, different materials can be deposited quickly and conveniently because the target can be substantially less than 1 mm on a side and 0.1 mm thick. This may be useful when different compositions or layered coatings[21] need to be explored in order to optimize a particular MFM tip characteristic (lateral resolution, moment, or coercive field). Once the optimal composition is found, a conventional sputtering target may be ordered for applications requiring large area films. Third, in our application we desire to coat the tip of the AFM lever while minimizing the material deposited on the rest of the cantilever. The additional deposit is undesirable because any metallic film that covers the whole cantilever will decrease the Q value of the lever in vacuum, reducing MFM sensitivity,[9] and may even short out the piezoresistive sensor that we use to measure cantilever deflection.

Needless to say, the financial considerations mentioned above do not take into account the initial investment required to purchase the FIB itself, which is substantially more than that of a simple sputtering system. The same is true for the operating and maintenance costs. In most cases it would be difficult to justify the purchase of an FIB for the sole purpose of depositing thin films over microscopic areas, but do we hope that this can be an additional incentive for the acquisition of a very versatile tool. In our case, as may be true in many laboratories nowadays, we are fortunate to have this tool available already so that the initial investment is not an issue. The FIB we use (FEI Strata DB235) is outfitted with a scanning electron microscope column, which provides a convenient means of aligning the cantilever and tip with the sputtering target.

Our MFM is a homemade instrument especially designed for low temperature experiments.[13][22] It utilizes commercially available microfabricated piezoresistive cantilevers. Our piezoresistive cantilevers were originally supplied by Marco Tortonese, then at Park Scientific Instruments, and later by Thermo Microscopes. We now purchase piezoresistive cantilevers from SII NanoTechnology Inc. (http://www.siint.com/), models PRC120 and PRC400 (sold in the USA by KLA-Tencor, http://www.ktnanopics.com/). Unlike standard cantilevers that can be purchased with a variety of magnetic coatings, piezoresistive cantilevers are only available uncoated. While this was the initial motivation for developing this technique, most of the benefits mentioned above would be relevant even for standard cantilevers that do not have a piezoresistive sensor.

3.2 Deposition Setup

Fig. 3.1 shows the basic geometry for our set up. For the initial demonstrations presented here, the AFM piezoresistive cantilever was mounted on the sample stage and the target was mounted on a nanomanipulator (Zyvex F100). Since the nanomanipulator is mounted on the same carriage as the sample stage, both are tilted together on the eucentric stage to allow alignment of the cantilever tip with the target under the guidance of the SEM. For deposition the eucentric stage is tilted so that the target normal is approximately 30° from the FIB axis, as shown in Fig. 3.1. We generally use a Ga+ ion beam current of 20 nA accelerated to 30 keV and a background gas pressure of 5×10^{-6} mbar. The FIB spot is usually rastered over a 20 μm by 8 μm area approximately 85 μm away from the AFM tip. Rastering is necessary to avoid milling a deep pit that tends to collimate the material sputtered off the target back in the direction of the ion beam. The view observed by FIB imaging during and after deposition is shown in Fig. 3.2. An added benefit of this deposition geometry, at least compared to conventional sputtering, is that only one side of the tip is coated, which results in higher lateral resolution compared to a tip that is coated on all sides.

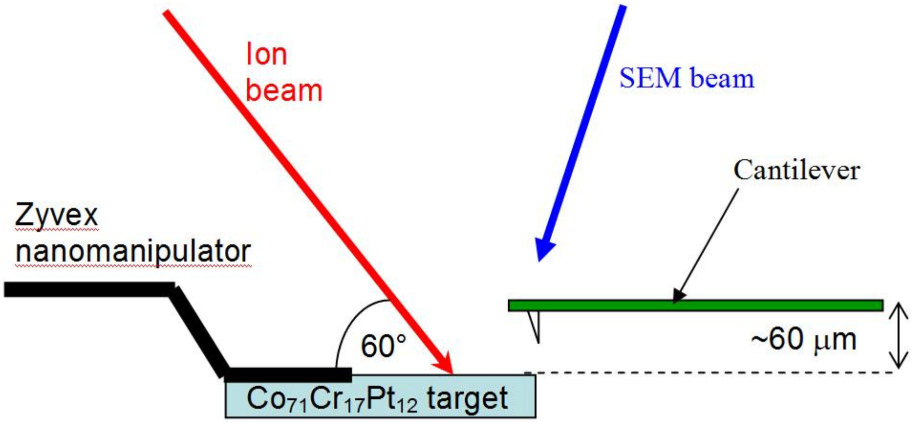

Figure 3.1: Diagram of the geometry used during FIB deposition or imaging procedures. The SEM beam is fixed in a vertical direction, while the FIB is fixed at 52° from the vertical. The cantilever and the nanomanipulator holding the target are mounted on a eucentric stage that is tilted to allow the SEM a better view during the alignment of the target and the cantilever.

Since the purpose of the SEM column in a dual-beam FIB system is usually to monitor the milling process, it is tempting to use the SEM to monitor the deposition. Unfortunately the amount of material we deposit is usually too

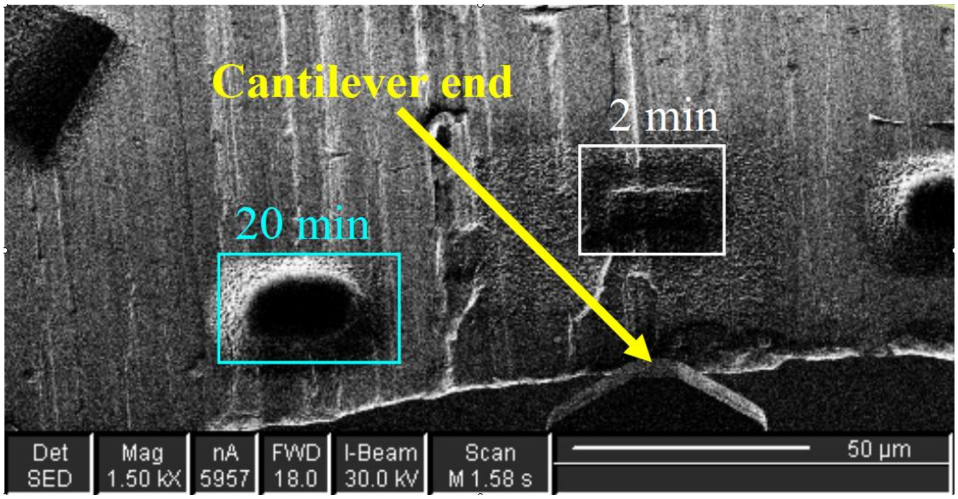

Figure 3.2: In-situ FIB image of the $Co_{71}Cr_{17}Pt_{12}$ target immediately after depositing on the cantilever for 2 min. The effect of the sputtering process on the target is highlighted with a rectangle. The cantilever end is lined up with the edge of the target, as sketched in Fig. 3.1. Most of the cantilever extends below this image. The location of the area that was ion-milled for 20 min to deposit on a separate cantilever is also visible.

little to give any contrast in the SEM, except perhaps for the thickest coatings reported here. Furthermore, in the present geometry (Fig. 3.1 and Fig. 3.2) the tip is under the cantilever during the FIB deposition procedure.

3.3 Deposition Characterization

Fig. 3.3 shows energy dispersive spectroscopy (EDS) results obtained in a different SEM. We deposited $Co_{71}Cr_{17}Pt_{12}$ for 20 minutes with the FIB on this cantilever. EDS shows that there is $Co_{71}Cr_{17}Pt_{12}$ deposited as far as 100 μm away from the tip. While this seems to be much further than desired, a cantilever on which we deposited $Co_{71}Cr_{17}Pt_{12}$ for only two minutes showed no evidence of $Co_{71}Cr_{17}Pt_{12}$ by EDS, even around the tip. However, we show below that this cantilever had excellent magnetic imaging properties. The tentative conclusion from these experiments is that EDS is not sensitive enough to detect the thinner magnetic coatings. Such coatings are thick enough on the tip to provide excellent imaging properties while being thin enough away from the tip area to minimize undesirable magnetic interactions or shorting of the piezoresistor. Optimizing the deposition geometry by, for example, bringing the cantilever tip closer to the target and increasing the angle by lifting the back of the cantilever will reduce the area of the deposit.

The EDS spectrum in Fig. 3.3 also shows the presence of Ga, which is a common contaminant in all FIB work. At this point we do not know if the Ga contamination deteriorates the magnetic properties of the deposit. While we plan future experiments to determine this, if the Ga does prove to be undesirable its incorporation can be reduced significantly by heating the cantilever during deposition. Since the vapor pressure of Ga is much higher than that of Co, Cr, or Pt, moderate heating to 100°C should make a big difference.

Optical techniques are also able to image the thicker (20 min) $Co_{71}Cr_{17}Pt_{12}$ deposit. Fig. 3.4 shows an optical micrograph of the cantilever obtained with a Nikon Optiphot Microscope equipped with Differential Interference Contrast (DIC). The area of the $Co_{71}Cr_{17}Pt_{12}$ deposit around the tip is clearly visible, extending to $\sim$120 μm away from the end of the cantilever, in agreement with the EDS results mentioned above. This deposit is also visible without DIC.

The thickness of the deposit can be estimated by measuring the shift in the resonant frequency of the cantilever, before (f_1) and after (f_2) the deposition. This technique is sensitive enough to detect mass changes in the attogram range with suitably designed cantilevers.[23] [24] The mass can be estimated assuming a simple harmonic oscillator: $m = k / (2 \pi f)^2$, where we use the value for the spring constant k = 3 N/m provided by the manufacturer. A more sophisticated analysis would take into account the geometry of the cantilever, which is effectively two beams in parallel with a mass attached at the end. However, since the thickness of the deposit is not uniform and the area is not well known, the simple estimate is sufficient for our purposes. For the 20 min $Co_{71}Cr_{17}Pt_{12}$ deposit we observed $f_1 = 37{,}112$ Hz and $f_2 = 33{,}664$ Hz, which gives $m_1 = 5.52 \times 10^{-11}$ kg and $m_2 = 6.71 \times 10^{-11}$ kg. Estimating that the area of the deposit is 2.5×10^{-9} m^2 and its density is 104 kg/m^3, the estimated thickness is 0.5 μm. We expect that the deposit on the tip is thicker than the deposit on the cantilever because the angle of deposition is closer to the local normal on the front side of the tip. Our thickness estimates may be off by a factor of 2 or 3, but in the end what matters is the performance of the MFM tip, as shown below.

For the 2 min $Co_{71}Cr_{17}Pt_{12}$ deposit we observed $f_1 = 42{,}927$ Hz and $f_2 = 42{,}829$ Hz, which gives $m_1 = 4.128 \times 10^{-11}$ kg and $m_2 = 4.147 \times 10^{-11}$ kg, yielding a thickness estimate of about 10 nm, which is sufficient to produce magnetic properties in this material.[25] [26] While this is too thin to be detected by EDS or standard optical techniques, it is sufficient to produce excellent MFM images, as shown in Fig. 3.5.

In the future we will measure the mass added during the deposition in situ by monitoring the cantilever's frequency shift in real time. This requires two electrical leads to measure the resistance of the cantilever, which is a measure of its deflection, and two leads to actuate a piezoelectric driver to excite the resonance of the cantilever. We have also built a simple jig that aligns up to five cantilevers with five corresponding targets independently under the guidance of an optical microscope. Once the alignment is accomplished, the jig is placed in the sample holder of the FIB. This cuts down on the user's time at the FIB and makes the in-situ nanomanipulator unnecessary.

3.4 MFM Results

The performance of these coatings for magnetic imaging is shown in Fig. 3.5 and Fig. 3.6, where the sample is a computer hard disk with in-plane magnetized regions. Typically, we expect to see strong contrast at the boundaries of these regions where the out of plane stray field and its gradient are the strongest. Figure 5 shows a typical high lateral resolution MFM image taken with the cantilever with a 2 min $Co_{71}Cr_{17}Pt_{12}$ deposit. The details observed in this image have not been seen before with piezoresistive cantilevers. The images compare favorably with published images obtained with commercial cantilevers tips coated with CoCr.[27] As a more valid comparison we have imaged the same hard disk with a commercial cantilever (MESP from

Veeco, coated with CoCr), resulting in the image shown in Fig. 3.6. Clearly the $Co_{71}Cr_{17}Pt_{12}$ FIB deposit gives better results. To illustrate the difference between different FIB coatings, Fig. 3.7 displays the MFM images obtained on the same hard disk with a piezoresistive cantilever coated with permalloy ($Ni_{80}Fe_{20}$) by FIB deposition for 30 min. The broadened bit transitions in this image may be due to the lower coercivity of permalloy and/or the thickness of the magnetic coating.

Higher resolution can be obtained by using more sophisticated coatings and by shaping the tip or the deposit on the tip with FIB. Liu et al., for example, used FIB to sharpen an AFM tip, then deposited Ta(3nm), NiFe(20 nm), FeMn(20 nm), and CoFe(20 nm) ex situ.[28] Phillips et al., on the other hand, first evaporated Co on a pyramidal tip and used FIB to remove most the Co, leaving a Co needle that acts as a magnetic monopole. With a similar process, a dipole tip was made by Litvinov and Khizroev.[29] Resolution as high as 11 nm has been achieved by FIB sharpening of a CoPt film deposited on a commercial cantilever tip by Gao et al.[30] Tips with carbon nanotubes have been coated with Co[31] and with CoFe,[32] both producing excellent results. We believe that in all these procedures the coating and the etching can be done within the FIB, with the advantage of having more sophisticated coatings available and doing all the processing in a single instrument. Sophisticated techniques may be used to characterize the magnetic properties of these tips.[33] [34]

In summary, we have demonstrated a convenient technique for making tips for magnetic force microscopy by sputter-depositing magnetic material with a focused ion beam. This technique is useful for depositing complex, expensive, or multilayer coatings in a quick and easy manner.

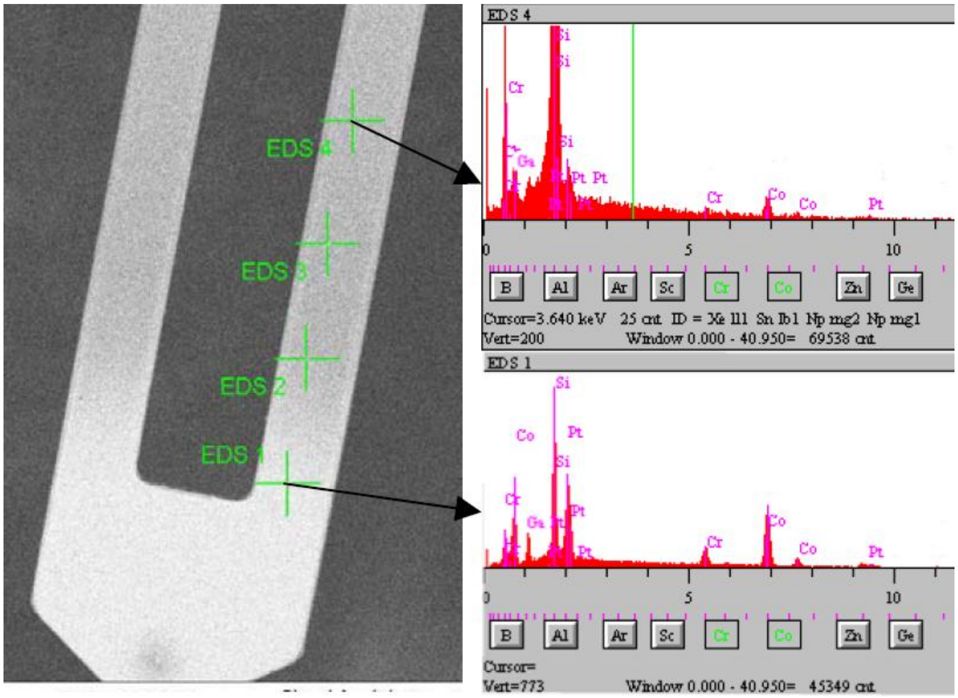

Figure 3.3: Ex-situ SEM image of a cantilever on which $Co_{71}Cr_{17}Pt_{12}$ was FIB-deposited for 20 min. This SEM is equipped with energy dispersive spectroscopy (EDS). Spectra were taken at the four locations marked with crosses. Two of these spectra are shown, where the decay of the EDS signal for Co, Cr and Pt is evident as the distance increases from the end of the cantilever. Ga contamination from the FIB is also detected. The cantilever with a 2 min deposit showed no EDS evidence of the elements deposited, although it had enough material to have excellent magnetic properties, as displayed in Figure 5.

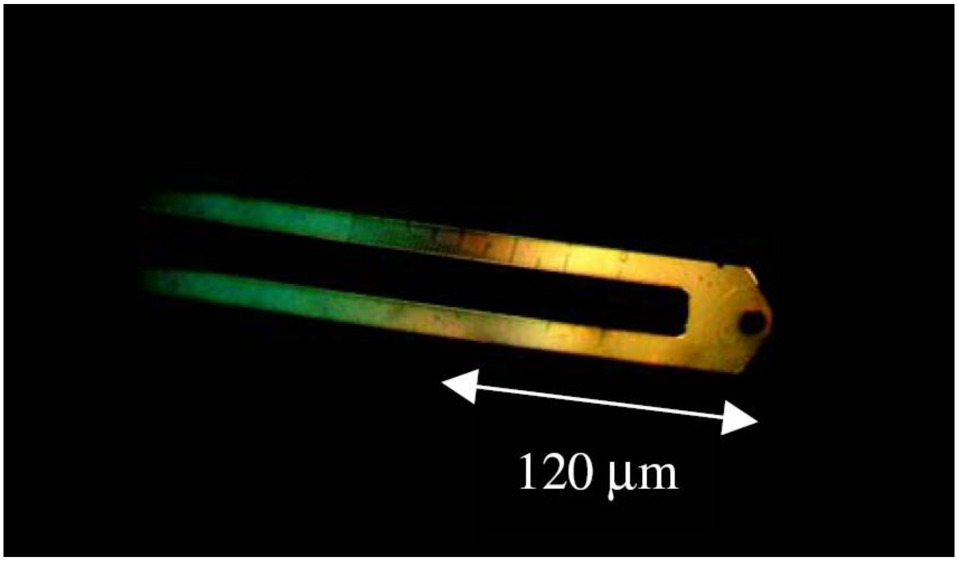

Figure 3.4: Optical micrograph of a cantilever on which $Co_{71}Cr_{17}Pt_{12}$ was FIB-deposited for 20 min. The change in color towards the end of the cantilever is due to the deposit, which extends $\sim$120 μm from the end

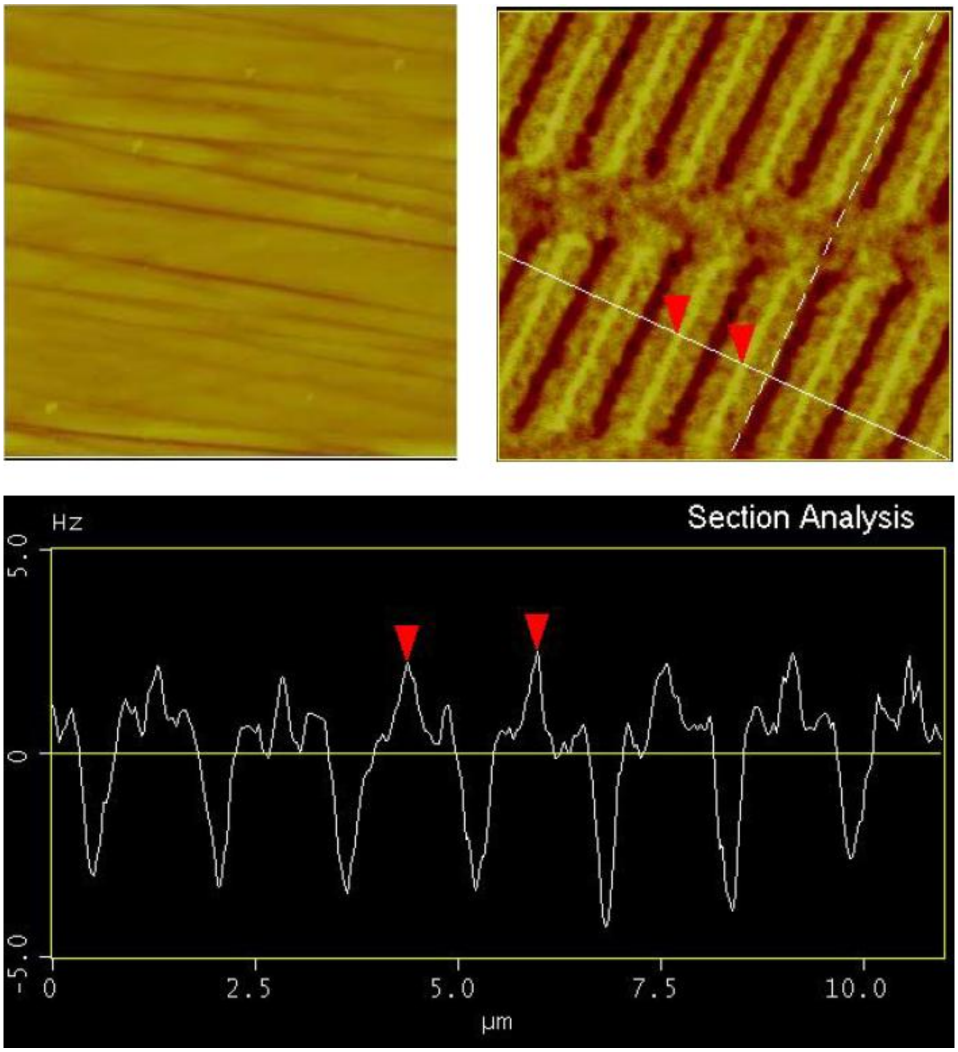

Figure 3.5: Topographic (left) and MFM (right) images of a computer hard disk taken with the cantilever/tip (shown in Fig. 3.2) that had $Co_{71}Cr_{17}Pt_{12}$ FIB-deposited for 2 min. We magnetized the tip perpendicular to the cantilever with a 1 Tesla electromagnet. The scan size is 10 μm × 10 μm with a topographic total range of 60 nm. The MFM image was taken with a lift height of 70 nm and the color scale spans a frequency shift of 10Hz. We obtain similar frequency shifts with Veeco's MESP-LM cantilevers, which have a moment of 0.3×10^{-13} emu according to the manufacturer. We therefore estimate the moment of this $Co_{71}Cr_{17}Pt_{12}$ coated cantilever to be similar. The section analysis taken along the white line marked in the MFM image shows the expected sharp peaks and dips at the boundaries between recorded bits as well as other fine features.

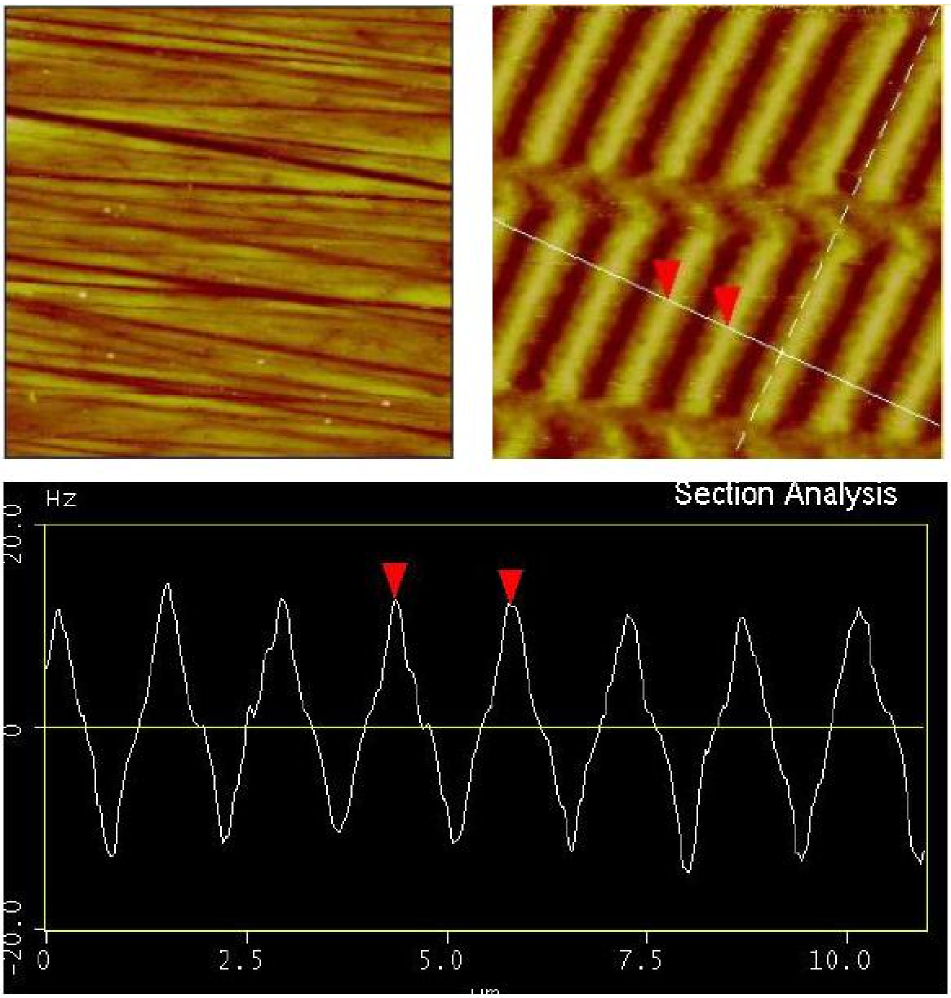

Figure 3.6: Topographic (left) and MFM (right) images of a computer hard disk taken with a commercial cantilever/tip (MESP from Veeco, coated with CoCr). We magnetized the tip perpendicular to the cantilever with a permanent magnet provided by the manufacturer, with an estimated field of 0.5 Tesla. The scan size is 10 μm × 10 μm with a topographic total range of 80 nm. The MFM image was taken with a lift height of 80 nm and the color scale spans a frequency shift of 40Hz.

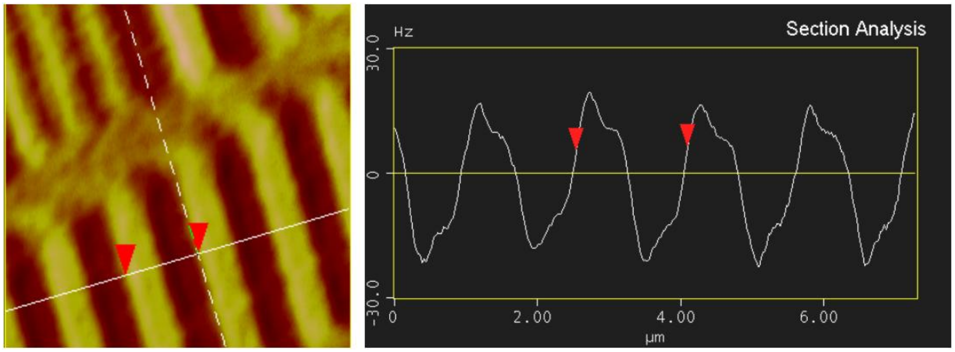

Figure 3.7: 7 μm × 7 μm MFM image of a hard disk taken with a cantilever/tip with a permalloy coating. We magnetized the tip perpendicular to the cantilever with a 1 Tesla electromagnet. This coating was deposited by FIB by sputtering an area of 20 μm × 8 μm for 30 min with an emission current of 20 nA. The deposit caused a frequency shift of -4.4 kHz in the resonance of the cantilever, which corresponds to a mass addition of approximately 10^{-11} kg or a deposit thickness of 0.4 μm. The qualitative and quantitative differences between this image and the one shown in Fig. 3.5 are due to the different magnetic properties of $Co_{71}Cr_{17}Pt_{12}$ and permalloy. This illustrates the importance of being able to deposit different materials on MFM tips.

Chapter 4

Magnetic Study of CMR Film

4.1 Introduction

$R_{1-x}A_xMnO_3$ (R is a trivalent rare-earth ion and A is a divalent dopant) materials such as $La_{0.67}Ca_{0.33}MnO_3$ (LCMO) change their electrical resistance by orders of magnitude more than conventional materials on the application of a magnetic field.[35] [36] These colossal magnetoresistance (CMR) materials also show hysteresis in their low-field magnetoresistance.[37] [38] Here we report observations of the magnetic domain structures using a variable low-temperature magnetic force microscope to understand the low-field MR effect.

4.2 Experiment

The $La_{0.67}Ca_{0.33}MnO_3$ film was grown by DC sputtering. The sputtering target source was made from La_2O_3, $CaCO_3$, and MnO_2. They were mixed and fired in air at 950°C for 12h to decarbonate. The product was then ground and pressed, then sintered at 1200°C for 24h in air. The resulting pellets were re-ground and fired at 1200°C for another 24h and slow-cooled at the rate of 5°C/min. The 150nm thick film was deposited on a $SrTiO_3$(001) substrate in 3.5 mbar pure oxygen as sputtering gas. The deposition rate was approximately 1.5 nm/min. An X-ray diffraction (XRD) pattern was measured using a Bruker-Nonius D8 Power Diffractometer with Cu Kα radiation (wavelength $\lambda = 0.15405$ nm). Fig. 4.1 shows the XRD pattern for the 150nm thick $La_{0.67}Ca_{0.33}MnO_3$ film. The XRD peaks from the substrate are identified with a star symbol. Near the substrate peaks, the (00n) peaks from the LCMO film are also observed. This lattice mismatch causes strain in the LCMO film, which in turn makes the magnetic easy axis lie in the plane of the film.[39]

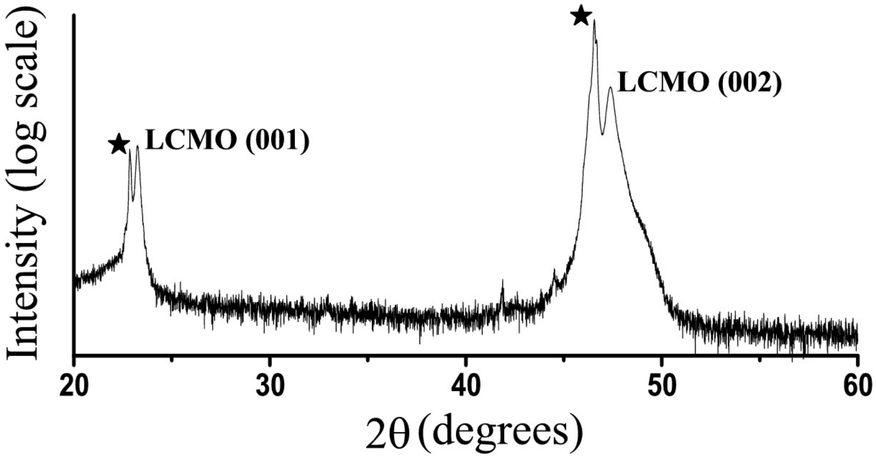

Figure 4.1: XRD pattern in scale for $La_{0.67}Ca_{0.33}MnO_3$ film deposited onto $SrTiO_3$ substrate by DC sputtering. The substrate peaks are marked with a star symbol.

The resistance and magnetic moment versus temperature are shown in Fig. 4.2(a). Around 260 K, the resistance starts to decrease and the magnetic moment to increase, indicating a phase transition temperature that is a good agreement with the bulk value.[40] Fig. 4.2(b) shows M-H loops measured at 80 K, 200 K, and 250 K. The transport data was measured in situ with our home-made low temperature Magnetic Force Microscope (MFM)[13]. The temperature dependent magnetization and magnetic hysteresis loop measurements were performed using a Quantum Design SQUID magnetometer.

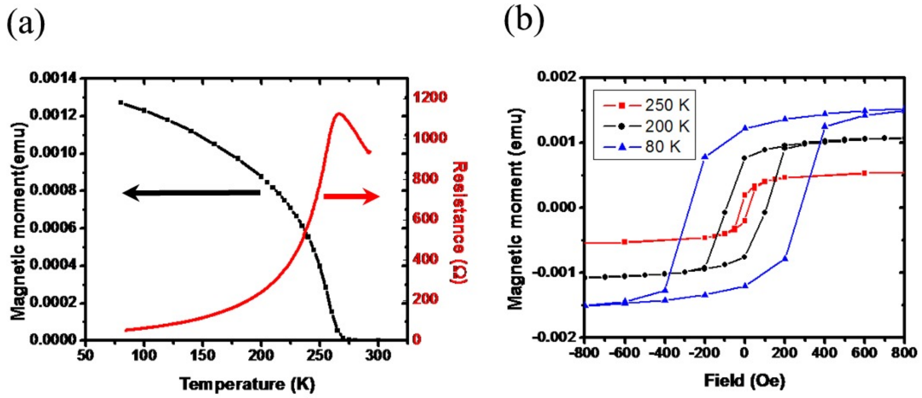

Figure 4.2: (a) Temperature dependence of the resistivity and magnetization of 150nm-thick $La_{0.67}Ca_{0.33}MnO_3$ film. (b) Parallel M-H loops at different temperatures.

We investigated the magnetic domain structure while changing the external field. We made an MFM tip with a relatively high coercivity by coating $Co_{71}Cr_{17}Pt_{12}$ on a piezoresistive cantilever (model PRC 400 from SII NanoTechnology Inc.) using our FIB sputtering method [41]. Before measuring the LCMO sample, we checked that the MFM image of a hard disk with CoCrPt coated tip did not change when we applied an external field up to 300 Oe at room temperature. We set the MFM measurement temperature as 200 K since the external field of 300 Oe is enough to saturate the LCMO film at 200 K, as shown in Fig. 4.2(b).

4.3 Result

Fig. 4.3 shows the MFM images of the LCMO sample with the scan size of 12 μm × 12 μm. We applied the external field parallel to the film plane in the direction indicated by the white arrow in Fig. 4.3(a). The external field values of the MFM image in Fig. 4.3(a) $\sim$ (f) are 288 Oe, 0 Oe, 44 Oe, -88 Oe, -144 Oe, and 331 Oe, respectively. In the MFM image, the dark contrast corresponds to an attractive interaction and, conversely, the bright contrast indicates a repulsive interaction, given that the magnitude of the force on the tip decays with increasing distance from the surface.[42] The MFM image features are pinned; they did not move much when we applied up to 330 Oe. The MFM image contrast inverted when the external field direction was reversed. Fig. 4.3(g) and (h) show the field dependence of the resistance and the magnetic moment. We then changed the external field direction and observed the effects with MFM images, as shown in Fig. 4.4. The image patterns are almost the same as in Fig. 4.3. The external field in Fig. 4.4 (a) and (b) is 288 Oe and 331 Oe respectively. The strain in the LCMO film has dominant role in the MFM image pattern. We consider that the strain comes from the lattice mismatch between the LCMO film and the STO substrate. As shown in Fig. 4.4(c), the MFM pattern and the defects in the topography are well matched. The defects in topography should be from lattice mismatch. The strain also provides the pinning sites in the MFM images. We propose that the low-field magnetoresistance hysteresis in the $La_{0.67}Ca_{0.33}MnO_3$ film is related to spin dependent tunneling effect, as observed by other groups for single grain boundaries.[43] [44] The LCMO film has the ensemble of the tunneling structures due to defects in the film. Each part in the LCMO film has different coercivity but mostly around the film coercivity, resulting that smooth hysteresis compared to the sharp hysteresis pattern of a single domain wall[43].

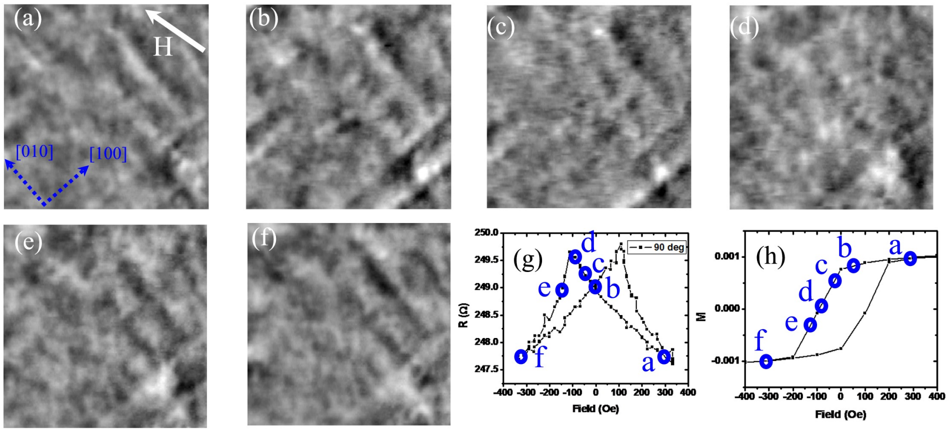

Figure 4.3: MFM images of one area of the sample (12 μm × 12 μm) at various in-plane directional magnetic field at 200K. The external field values of the images are : 288 Oe (a), 0 Oe (b), -44 Oe (c),-88 Oe (d),-144 Oe (e), -331Oe (f). The white arrow in the (a) indicates the direction of the external field. Field dependence of the resistance (g) and magnetic moment (h).

We expected the four-fold in-plane magnetocrystalline anisotropy, as observed by O'Donnell et. al. Fig. 4.5 shows the vibrating sample magnetometer (VSM) data of the LCMO film at 96 K. Fig. 4.5(b) shows the remanent magnetization on the sample axis having angle with respect to an applied field axisdirection. This indicates that there is no obvious in-plane anisotropy. This result is confirmed in Fig. 4.5(c), showing M-H loop for different applied field

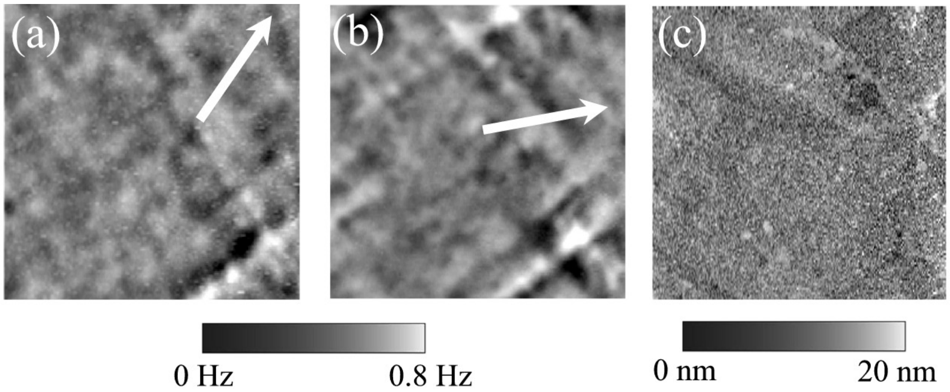

Figure 4.4: MFM images (a, b) and topography (c) at the same position. All MFM images in Fig. 4.3 were also measured at the same position. The white arrow shows the applied field direction. The external field in (a) and (b) is 288 Oe and 331 Oe respectively.

directions. The coercivity and remanent magnetization did not change much in Fig. 4.5(c). From all this we conclude that there is no measurable in-plane anisotropy in our films.

4.4 Summary

We made the 150nm thick LCMO film on STO substrate. By XRD and SQUID magnetometer, we verified that this film shows similar properties as reported other group. We measured transport data and magnetic domain structure simultaneously using low temperature MFM to investigate the magnetoresistance hysteresis in $La_{0.67}Ca_{0.33}MnO_3$ film. We propose that the hysteresis is the result from the ensemble of magnetic domain changes according to external field. Moreover the magnetic domains are pinned around the

LCMO film defects.

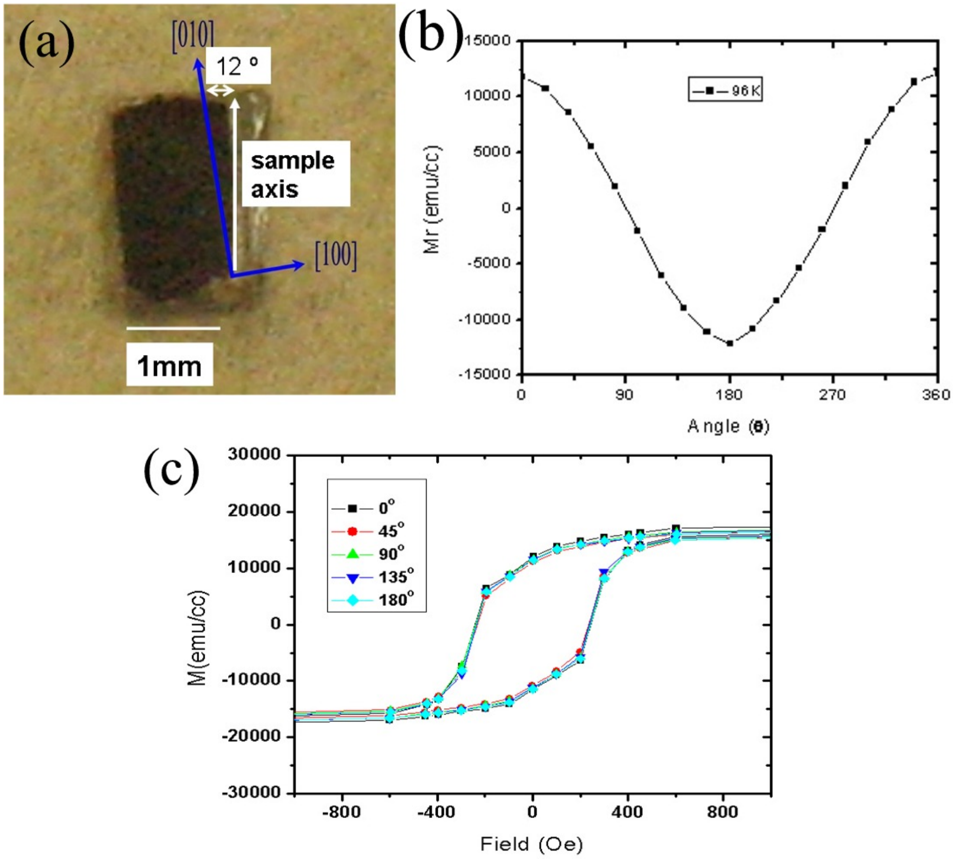

Figure 4.5: (a) Photograph of a LCMO sample used in VSM measurement. White axis represents sample axis. (b) remanent magnetization (M_r) plotted as a projection on the sample axis. The angle θ is the angle in the film plane between sample axis and applied field direction. (c) magnetization moment measured along the field axis.

Chapter 5

Sintering Effect of Annealed FePt Nanocrystals

Nanometer-size magnets are of great interest to industrial and scientific researchers due to their need for high-density storage media. For high-density magnetic information storage, material with high uniaxial magnetocrystalline anisotropy is needed to overcome the superparamagnetic effect.[45] FePt alloy is one of these storage media candidates.[45] Chemically synthesized and self-organized FePt nanoparticle arrays exhibit high coercivity, as much as 4 kOe at room temperature, when these nanocrystals are annealed.[46] But annealing can induce agglomeration and sintering of monodisperse FePt nanocrystals.[47] [48] [49] [50] [51] The sintering temperature at which agglomeration occurs depends on the size and stabilizers of the nanoparticles.[47] [48] [49] Magnetic force microscopy [52] (MFM) is a useful tool to map the mesoscopic magnetic properties of thin magnetic films, providing a snapshot of local magnetization phenomena that give rise to the macroscopic properties of the film. MFM has been used in several studies including cobalt nanoparticle assemblies [53], sputtered nanocluster films [54] [55] [56] [57], and annealed self-assembled FePt nanoparticles [58].

5.1 Nanocrystal Synthesis and Assembly

FePt nanocrystals were made by the high temperature reduction of a platinum (Pt) precursor and thermal decomposition of an iron (Fe) source in the presence of capping ligands.[59] At room temperature, platinum acetylacetonate (0.5 mmol) was mixed with 1,2-hexadecanediol (1.5 mmol) in dioctylether (20mL) in a three-neck flask. The mixture was agitated at room temperature while flushing with nitrogen for $\sim$20 min. The mixture was then heated to 100°C, at which point iron pentacarbonyl (1 mmol), oleic acid (0.5 mmol), and oleylamine (0.5 mmol) were injected, and the resulting mixture continued to be heated to the refluxing temperature of dioctylether. The reaction mixture was held at the refluxing temperature for 30 min, and was allowed to cool to room temperature by removing the heating element. The solution was collected and centrifuged at 8000 rpm for 10 min. Poorly capped particles and very large nanocrystals form a precipitate that is discarded. The supernatant was then mixed with 20 mL of ethanol to precipitate the FePt nanocrystals and separate them from organic molecular byproducts. The nanocrystals were collected as a precipitate after another centrifugation at 8000 rpm for 10 min. For the MFM studies and magnetic measurements, the nanocrystals were precipitated one more time from chloroform using ethanol as the antisolvent to obtain a clean sample with minimal organic byproducts and free capping ligands. The nanocrystals redisperse in a variety of organic solvents, including chloroform, toluene and hexane. The Pt concentration was estimated to be 40-48% based on the observed formation of the FCT phase and the strong magnetic properties of thicker films [46], as shown below.

Samples for MFM and SQUID measurements were spin cast onto mica substrates and samples for x-ray diffraction were spin cast on a silicon wafer to make uniform films. TEM samples were prepared by drop casting dilute FePt dispersions onto a carbon-coated copper grid. These films were annealed in a quartz tube furnace while flowing helium or purified nitrogen gas through the tube.

5.2 MFM Study

Atomic force microscopy (AFM) and MFM images were simultaneously obtained using a Digital Instruments Multimode microscope operated in Tapping/Lift mode under ambient conditions. Fig. 5.1 shows the annealing effects on a 12nm-thick FePt film. Fig. 5.1(a) and 5.1(b) are the AFM and corresponding MFM images, respectively. The morphology and magnetic image of the sample after annealing is shown in Fig. 5.1(c) and 5.1(d), respectively. The height range of AFM images in Fig. 5.1 is 15nm and the phase range of the MFM images is 1 degree. This phase range is a measure of the strength of the magnetism of the sample (and the MFM tip), ranging from zero for nonmagnetic material up to 15 degrees for a computer hard drive. The lift height in Fig. 5.1(c) and 5.1(d) is 30nm. Fig. 5.1 was taken using MESP-type MFM tips purchased from Digital Instruments. These tips have a Co-Cr coating with a medium moment ($\sim 10^{-13}$ emu) and coercivity ($\sim$400 Oe). All of the images in Fig. 5.1 are taken in the same location. After annealing at 605°C for 30 min, there was some change in topography, but most of the features remained, with a typical reduction of the film thickness by 25%. Since there was also lateral shrinkage, we could find cracks, from which we could measure the thickness of the film. The difference in the MFM images in Fig. 5.1(b) and 5.1(d) is evident. However, we could not observe the pattern of MFM images shown in Fig. 5.1(d) everywhere on the film after annealing. At some positions we saw MFM images similar to Fig. 5.1(b), indicating that the film thickness or the sintering effects are not uniform.

Fig. 5.2 shows MFM images of films with different thicknesses. Fig. 5.2(a) is recorded after re-annealing the sample shown in Fig. 5.1(c) at 630 °C for 30 min to improve its magnetic properties. The MFM contrast increased and became clear compared with Fig. 5.1(d). MFM images of thicker films annealed at 630 °C for 30 min are shown in Fig. 5.2: (b) 20nm, (c) 32nm, and (d) 55nm. The MFM signal becomes stronger with increasing thickness as expected. Since each image is optimized individually, the parameters are not the same, making quantitative comparisons difficult. Nevertheless, it is valid to compare MFM images taken with similar lift height. Accordingly, the MFM signal in (d) is stronger than the signal in (b) and the signal in (c) is stronger than (a), as one would expect from thicker films. The qualitative shape and size of the patterns in the MFM image, however, did not change much. When we scanned the sample shown in Fig. 5.2(a) at zero external field after applying a 1 Tesla external field perpendicular to the film plane, the MFM image did not change, indicating no magnetic remanence in the film or a coercivity below the field applied by the tip (∼400 Oe). Furthermore, the MFM pattern in Fig. 5.2(d) did not change when we scanned with a 3000 Oe external field applied in the perpendicular direction.

5.3 SQUID, TEM, and X-ray Studies

To understand the MFM images shown in Fig. 5.2, we measured the parallel and perpendicular M-H loop of the 55nm-thick film shown in Fig. 5.2(d) at 300 K with a SQUID magnetometer. Fig. 5.3(a) and (b) are the magnetization data after subtracting the M-H loop of a mica substrate of the same size. We also took MFM images of the same film shown in Fig. Fig. 5.2(d) by magnetizing a high moment ($>3\times10^{-13}$ emu) HM-MESP tip purchased from Digital Instruments upward and downward as shown in Fig. 5.3(e) and (f). The MFM image in Fig. 5.3(c) was taken when the magnetization direction of tip is upward, while the image in (d) was taken after reversing the magnetization direction of tip. The positions marked "1" and "2"in (c) and (d) represent the same location. The bright spots marked "2" are due to contamination.

A careful examination of the MFM images in Fig. 5.3(c) and 5.3(d) shows that the magnetic patterns did not change. For comparison we tested a video tape having higher coercivity: when we changed the magnetization direction of the MFM tip, the dark and bright patterns also reversed. From this we conclude that the 52 nm FePt film has a coercivity lower than the field applied by the tip, which is estimated to be 400 Oe for a lift height of 50 nm

[60]. The magnetic contrast is not reversed because the tip magnetizes the film on a local scale.

When we measured all films with LM-MESP type MFM tip from Digital Instruments, we could not see any MFM contrast. We believe that the magnetic moment of the LM-MESP tip ($\sim 0.3 \times 10^{-13}$ emu) is too low to give a measurable signal on films with low magnetic moment.

Having concluded that the thin films of FePt nanocrystals have very low or zero coercivity and remanent magnetization, we believe that the MFM image contrast should relate to the non-uniform areal density of the FePt due to sintering [48] [51]. The dark parts in the MFM images correspond to a higher areal density of sintered FePt. Fig. 5.4(a) shows the TEM image of the FePt nanocrystal monolayer before annealing. Before we annealed a bilayer (approximately) FePt nanocrystal film, the density distribution in the TEM image was almost uniform, as shown in Fig. 5.4(b). After annealing the sample of Fig. (b), the spatial density distribution became non-uniform as in Fig. 5.4(c) and (d). Since the lateral resolution of the MESP tip is greater than $\sim$40 nm, sintered nanocrystals that are grouped closer than 40 nm are averaged to a single feature in the MFM image.

X-ray diffraction measurements provide further evidence of sintering. The crystallite size can be determined from the Scherrer formula $B = 0.9/(D \cos\theta)$, where B is the broadening of the diffraction line measured at half of its maximum intensity in radians, is the wavelength of the X-rays, D is the average diameter of crystal particle, and θ is the Bragg's diffraction angle [61].

Fig. 5.5 shows XRD patterns for a ∼250nm-thick FePt film. The sharp peaks in the XRD patterns are due to the silicon substrate. The locations of the sharp peaks are different before and after annealing since the azimuthal angles of incident X-ray are different. Fig. 5.5(a) is the pattern before annealing the sample. From the Scherrer formula, using the (111) peak, the average crystal size before annealing is ∼3.8 nm. This value is in good agreement with the TEM result shown in Fig. 5.4(a). Fig. 5.5(b) is the pattern after annealing for 30 min at a temperature of 605 °C. After annealing, the thick film had a sharper (111) peak resulting from an increase in the crystallite size to 13 nm, producing a coercivity of 5.5 kOe at 300K, as shown in Fig. 5.6, which is consistent with previous findings for thick films [46]. Since the properties of our thicker films are similar to those reported in the literature, we conclude that the weaker magnetic properties of our thinner films are a consequence of their reduced thickness and not shortcoming of the source nanocrystals.[62]

The diffraction data analysis assumes only perfect nanocrystals, so there may be many particles that are twinned, with an overall size bigger than 13 nm. Furthermore, the MFM image displays a two dimensional projection of the magnetic particles as deep as 30 nm, so that MFM interprets many particles as one particle if they overlap in two dimensions even though they are separated in three dimensions. These considerations help to understand why the typical feature size in the MFM images shown in Fig. 5.2 is greater than 13 nm.

5.4 Summary

Chemically synthesized FePt nanocrystal thin films show low coercivity at room temperature after being annealed at temperatures in the range of 605-630°C for 30 min. We studied 12 to 55 nm thick films using MFM, SQUID, TEM, and x-ray diffraction. The patterns shown in the MFM images are likely due to the sintering of FePt nanocrystals and the high moment of the MFM tip. Thicker films show strong ferromagnetic behavior, as reported by other groups. The motivation to find thinner nanocrystal films with sufficiently strong magnetism for data storage applications is still strong. However, thinner films are more likely to be self-assembled into an ordered structure, which produces a smoother surface and a more uniform film.

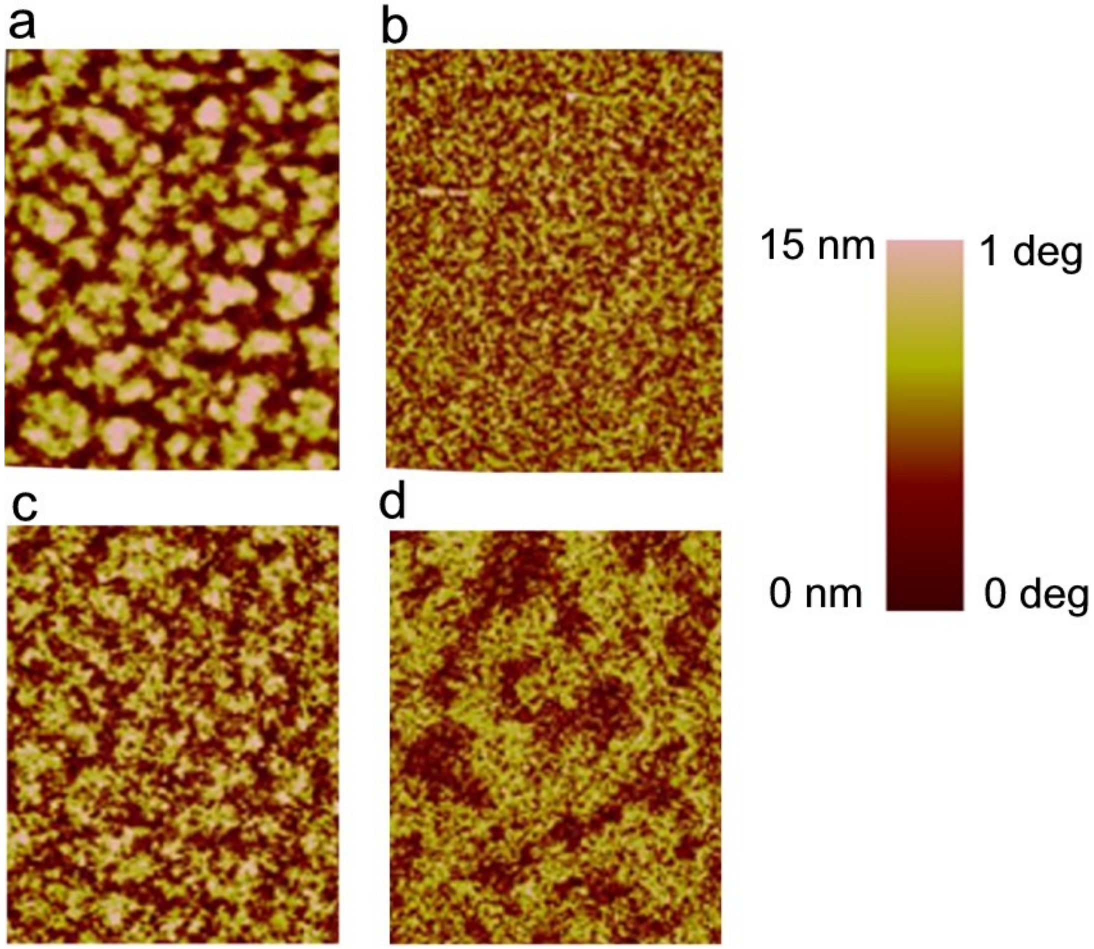

Figure 5.1: (a) AFM (4 μm × 5 μm) and (b) corresponding MFM image of un-annealed 12nm-thick FePt nanocrystal film. (c) AFM and (d) MFM image after annealing the 12nm-thick film at 605°C for 30 min. All images are taken on the same location.

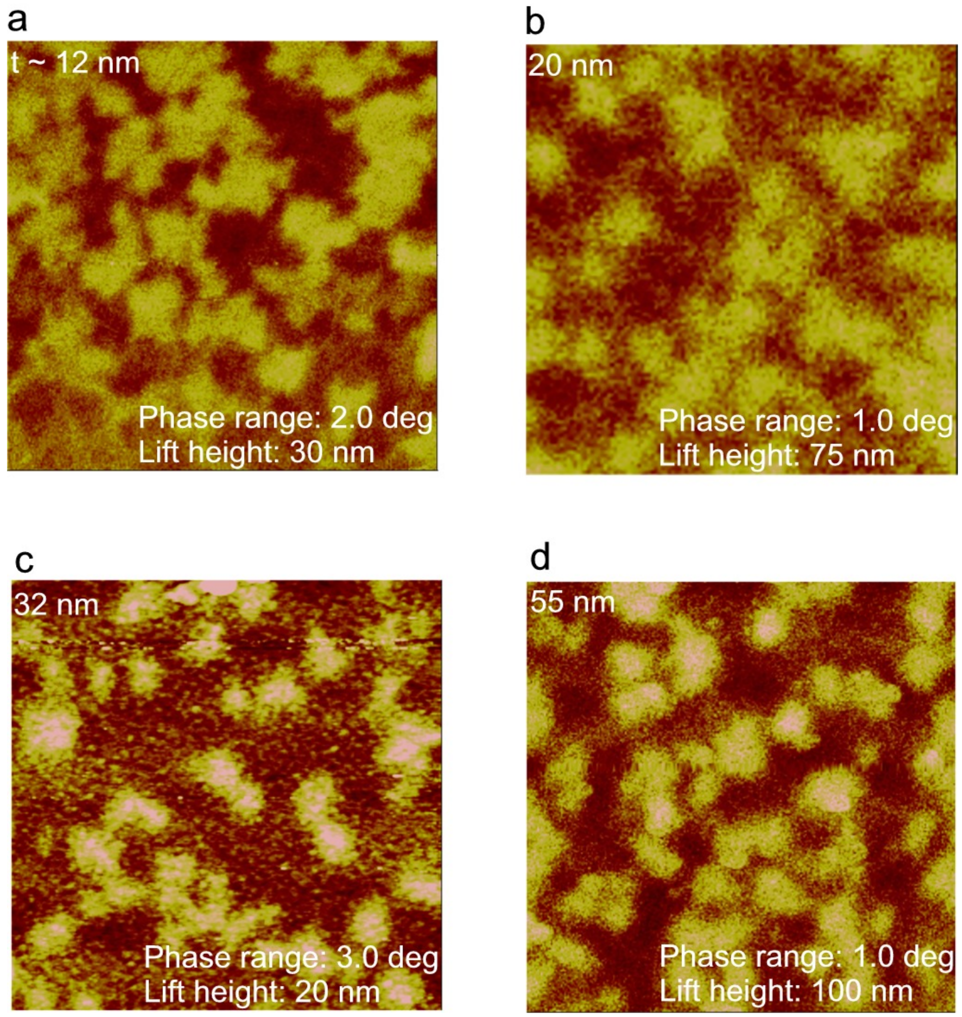

Figure 5.2: MFM(5 μm × 5 μm) images of FePt thin films with different thickness: (a) 12 nm, (b) 20 nm, (c) 32 nm, (d) 55 nm. The sample in (a) is the same as in Fig. 1(c) after being re-annealed at 630°C for 30 min. In (b), (c), and (d), samples are annealed at 630°C for 30 min.

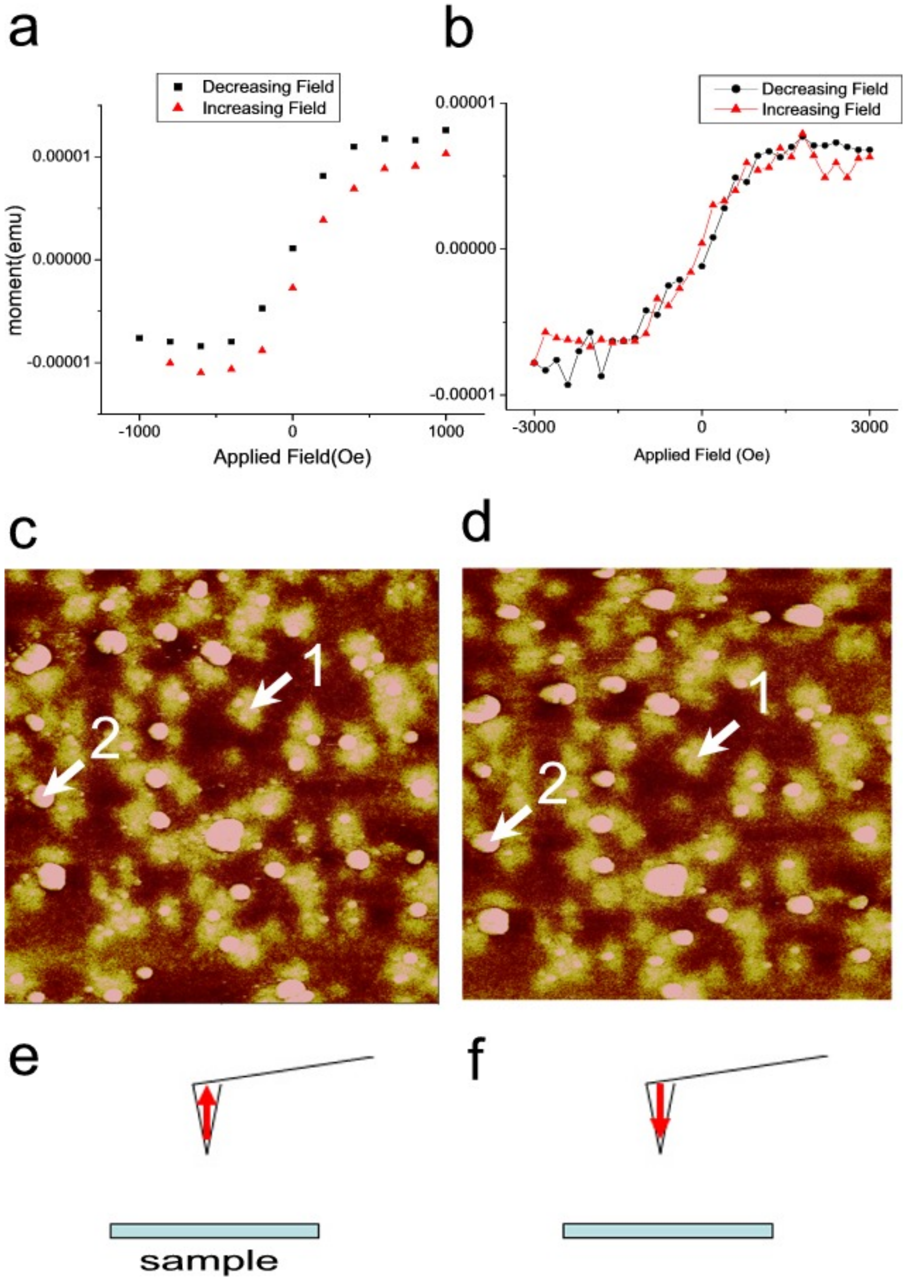

Figure 5.3: (a) Parallel and (b) Perpendicular M-H loop at 300K of the 50-nm-thick sample shown in Fig. 5.2(d). (c) MFM(5 μm × 5 μm) image is taken by HM-MESP MFM tip magnetized upward as shown in (e). (d) MFM image using HM-MESP tip magnetized downward as shown in (f).

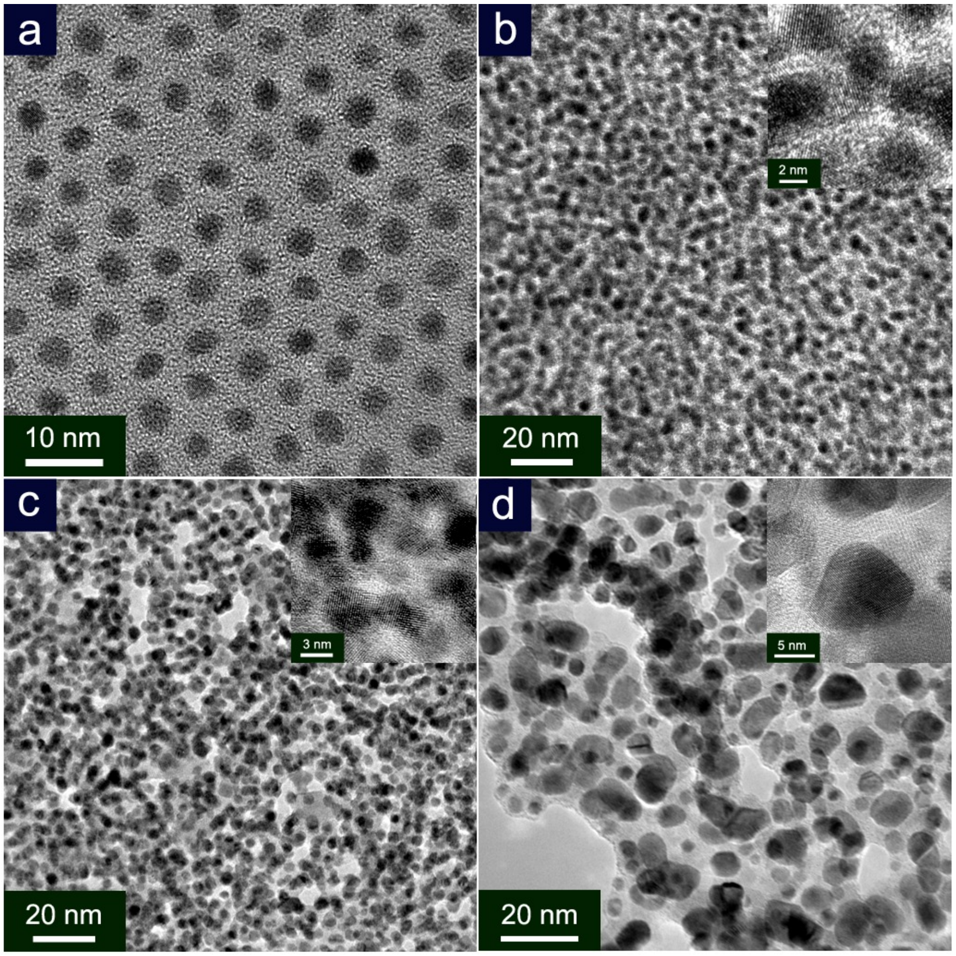

Figure 5.4: (a) TEM image of the un-annealed FePt nanocrystals. (b) TEM image of unannealed nanocrystal bi-layer on a TEM grid. (c) TEM image after annealing the sample of (b) at 580°C for 30 min, showing no significant coalescence. (d) TEM image after further annealing the sample of (c) at 630°C for 30 min, showing substantial coalescence.

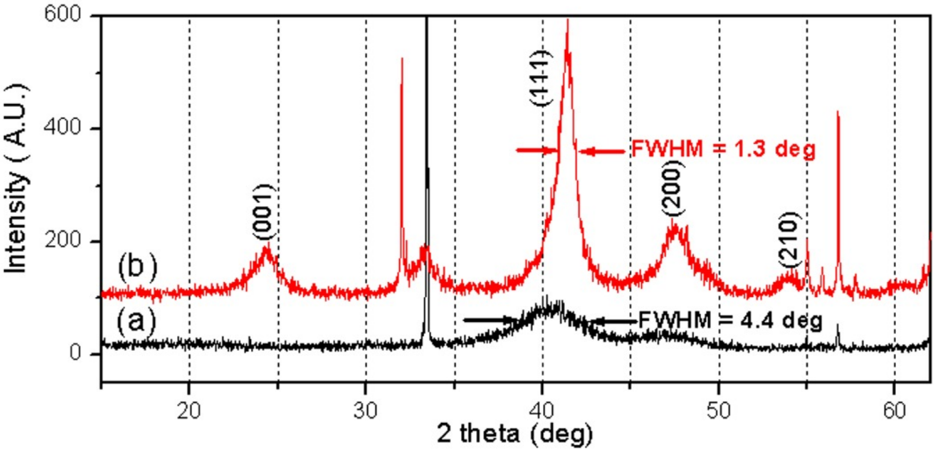

Figure 5.5: XRD patterns of FePt film with t= 250 nm (a) before annealing (b) after annealing for 30 min at a temperature of 605°C. The index is based on FCT FePt reflections. The diffraction patterns were collected with a Bruker-Nonius D8 Powder Diffractometer with Cu K_α radiation (wavelength $\lambda = 0.15405$ nm).

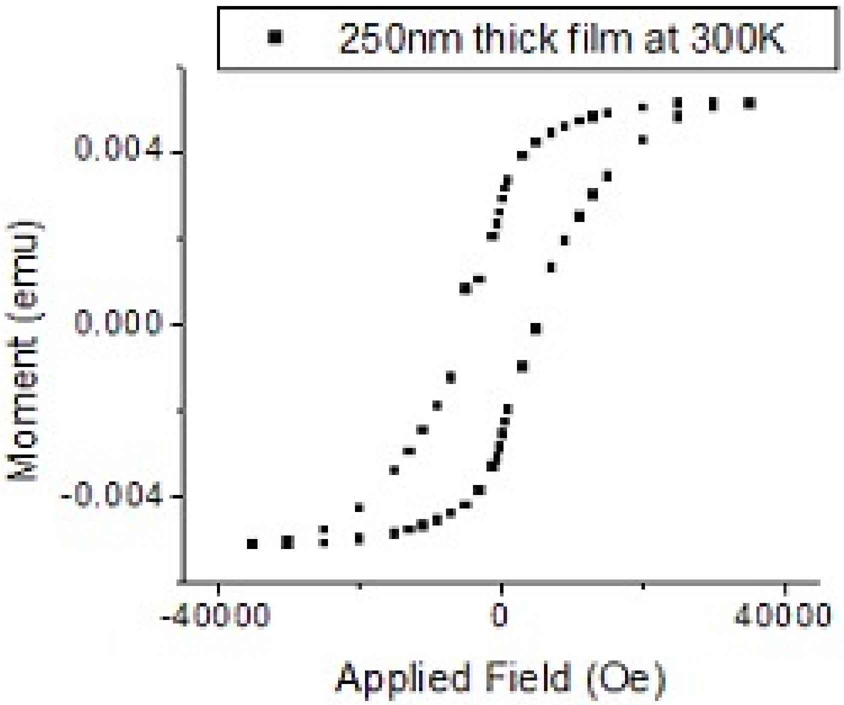

Figure 5.6: Parallel M-H loop of a 250 nm thick FePt nanocrystal film at 300K.

Chapter 6

Micromagnetic Study of FePt nanocrystals overcated with silica

Chemically-synthesized FePt nanocrystals must be annealed at a high temperature (>550°C) to induce the hard ferromagnetic $L1_0$ phase. Unfortunately, the organic stabilizer covering these nanocrystals degrades at these temperatures and the nanocrystals sinter, resulting in the loss of control over nanocrystal size and separation in the film as discussed in Chapter 5. We have developed a silica overcoating strategy to prevent nanocrystal sintering. In this study, 6 nm diameter FePt nanocrystals were coated with 17-nm-thick shells of silica using an inverse micelle process.

6.1 Synthesis and bulk characterization

To prevent sintering, a SiO_2 coating was developed.[63] [64] The thermal diffusion of Fe and Pt atoms remains confined within the SiO_2 shell during the heat treatment.[63] Precursor fcc FePt nanoparticles were prepared according to the method of Chen et al.,[65] and were subsequently coated by SiO_2 according to the method of Fan et al.[66], as we have described in detail in Ref. [64]. Fig. 6.1(a) shows a transmission electron microscopy (TEM) image of FePt nanocrystals overcoated with silica before annealing. The size of the FePt cores, as determined by TEM, is 6 nm and the average diameter of the silica coated nanocrystals is 39 nm with a standard deviation of 1.4 nm. The silica-coated FePt nanocrystals were deposited onto a silicon wafer to make films. The thinner films (100 nm and 900 nm) were made by putting a drop of nanocrystal solution on the substrate and using a spinner at 1,500 rpm. The 2.5 μm-thick films were made by drop casting (letting a drop dry on the surface). For some applications a glass substrate is preferred, but in our case the Si substrate provides a convenient flat surface and avoids possible charging problems that could affect the MFM images. These films were annealed at 700°C for 30 min in a quartz tube furnace while flowing N_2 (93%) / H_2 (7%) gas to convert the nanocrystals from the fcc structure into the $L1_0$ structure. We estimate an upper bound for the density of 1.4 g/cm^3 based on the dimensions of the particles, the densities of silica (2.6 g/cm^3) and FePt (14.7 g/cm^3), and by assuming a simple cubic packing of spheres. The actual density is likely to be lower, judging from the porosity observed in very thin films prepared for SEM analysis, as shown in Fig. 6.2. On the other hand, the porosity is exacerbated in these very thin films because the lateral shrinkage results in gaps, while for thicker films the gaps may be filled by shrinkage of the film thickness.

X-ray diffraction (XRD) measurements before and after annealing are shown in Fig. 6.1(b). After annealing the (111) diffraction peak shifts from $2\theta = 40°$ to a slightly higher angle and new peaks appear, such as the (110) peak at around $2\theta = 33°$, indicating a phase transition from fcc to $L1_0$. The nanocrystal size can be determined from the Scherrer formula $B = 0.9/(D \cos\theta)$ [61], where B is the broadening of the diffraction line measured in radians at half of its maximum intensity, is the wavelength of the X-rays, D is the average diameter of the crystalline particles, and is the Bragg diffraction angle. The peak breadth in the XRD patterns both before and after annealing is $\sim$1.35°, corresponding to an average diameter of $\sim$6.3 nm, which is in good agreement with the FePt size determined by TEM. Since the peak broadening in the XRD pattern did not change upon annealing, there is no agglomeration and coalescence of the FePt cores. We also point out that the XRD pattern in Fig. 6.1(b) is possible only if the c axes of the nanocrystals are randomly oriented. The chemical ordering of the $L1_0$ phase can be estimated based on the ratio of the (110) and (200) peaks,[61] [67] or using the lattice parameter ratio (c/a).[68] From these estimates, we calculate an order parameter S = 0.7-0.9 (which is defined as $S = [r_A - F_A]/[1 - F_A]$, where r_A and F_A are fractions of A atoms in the correct sites and in the alloy, repectively; S = 1 for perfect ordering)[61]. The chemical composition has been determined with TEM-EDS to be between 37% and 42% Fe content.

A superconducting quantum interference device magnetometer (SQUID) was used to characterize the magnetic properties of the nanocrystal composite film. Fig. 6.1(c) is a magnetic hysteresis loop at room temperature. The diamagnetic contribution to the hysteresis loop from the silica shells is negligible compared to the magnetic moment of the FePt cores, as determined by the

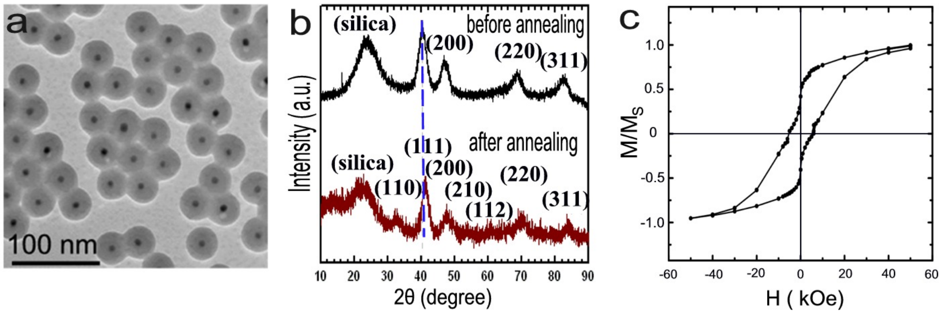

Figure 6.1: (a) TEM image of un-annealed FePt nanocrystals overcoated with a silica shell. The dark core is FePt and the lighter shell is silica. The average size of the FePt nanocrystals is 6 nm and the silica shell thickness is approximately 17 nm. (b) XRD patterns of FePt nanocrystals overcoated with silica shell before and after annealing for 30 min at a temperature of 700°C. The diffraction patterns were collected with a Bruker-Nonius D8 powder diffractometer with Cu K_α radiation (wavelength $\lambda = 0.15405$ nm). (c) In plane M-H loop at 300K of a 2.5-μm-thick film after annealing for 30 min at a temperature of 700°C. The saturation magnetization, MS, is 5 emu/cc, with an uncertainty of 20% due to the unknown packing fraction of these nanospheres and the nonuniform thickness of this drop-cast film. Furthermore, the M-H loop indicates that full saturation is not quite reached at 50 kOe, but this may be due to a slight error in the subtraction of the diamagnetic contribution from the silicon substrate, or to the fact that we have a composite with randomly oriented hard axes (see figure 7 in [69]).

following calculations. The saturation magnetization of bulk $L1_0$ FePt is about 1140 emu/cm^3.[45] Since the diameter of a FePt core is ∼6nm, the magnetic moment of one FePt nanocrystal is $\sim 1.0\times10^{-16}$ emu. The mass susceptibility and density of SiO_2 are -29.6 emu/(g·Oe) and 2.6 g/cm^3, respectively.[70] The diamagnetic moment from a 40 nm size silica sphere at 5 Tesla is $\sim 1.0\times10^{-20}$ emu, which is indeed negligible. In the M-H loop, the ratio of the remanent magnetization to the saturation magnetization is about 0.5. A possible expla-

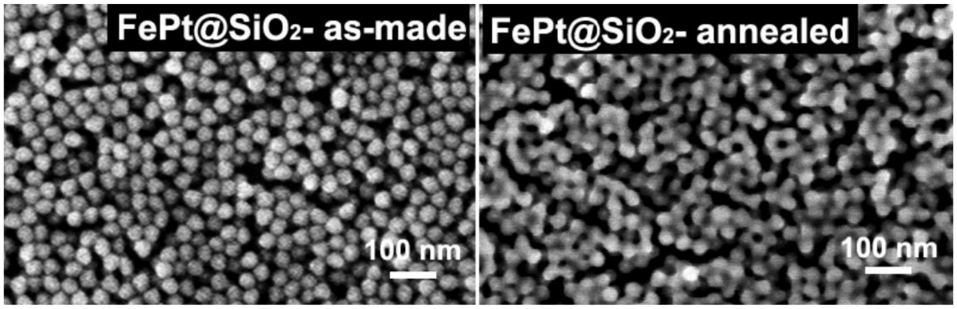

Figure 6.2: SEM images of FePt@SiO$_x$ nanocrystal films, a few layers thick, before and after annealing. These films were spin-coated on Si substrates.

nation for this is that the magnetic dipole interaction among single domain nanocrystals is weaker than the interactions between individual nanocrystals and the external field.

The shape of the M-H loop in Fig. 6.1(c) may be interpreted as evidence of having two phases present in the sample. Since we have no other evidence of the existence of a substantial fraction of another phase, this aspect is not well understood. This has been observed by other groups and is as yet unexplained.[71] [72]

6.2 Micromagnetic characterization

We studied the micromagnetic structure of these nanocrystal films with magnetic force microscopy (MFM), using a Digital Instruments Multimode microscope under ambient conditions. Fig. 6.3(a) shows part of an island in a 2.5 μm-thick film. We prefer to study islands or trenches because it is possible to get an accurate determination of the film thickness and a high magnetic contrast at the edges. The scanned area is 15 μm × 3.75 μm. The two possible directions of the magnetization of the MFM tip are also shown in Fig. 6.3(a). To manipulate the magnetization directions of the nanocrystal single domains, we applied an 8 Tesla ex-situ field to the left and to the right along the film plane, as well as in the up and down direction perpendicular to the film plane. After magnetizing the film with the 8 Tesla field, we scanned the same region around the island at zero field as shown in Fig. 6.3(c), (d), (e), and (f). All images in Fig. 6.3 were taken using an MFM tip (MESP from Veeco, coated with CoCr), magnetized downward.

We used the "floating mode," in which the MFM tip is rastered at a fixed distance from the average sample surface and the tip does not trace the topography of the sample. In this floating mode, the tip will trace a flat rectangle at a distance h from the film surface, as shown in blue in Fig. 6.3(b). Fig. 6.3(c), (d), (e), and (f) show the phase shift of the oscillating cantilever in the floating mode and the corresponding section analysis. The line profile in the section analysis is an average of the scans contained between the two white lines in the MFM image. The floating height from the surface of the nanocrystal composite film is h = 450 $\sim$ 600 nm, which is chosen to avoid crashing the tip into the film. In Fig. 6.3(c), the dark and bright contrast along the edges of the film represents a phase shift due to the interaction between the MFM tip and the FePt nanocrystals. The phase shift pattern shows that the film behaves like a magnetic dipole with field gradients of opposite sign on opposite edges.

The spatial resolution of the MFM tip is about ~30 nm and the film is composed of many layers of FePt nanocrystals. Therefore, we can see only the average effect of many FePt nanocrystals. The minimal stable grain size of $L1_0$ FePt for a storage time of t $\approx$ 10 years is 2.8 nm and the estimated magnetic single domain size in bulk FePt is 340 nm.[73] Consequently, a 6 nm-size $L1_0$ FePt nanocrystal must have a single domain structure that is stable at room temperature. The $L1_0$ phase has a uniaxial magnetocrystalline anisotropy with the easy axis along the c axis.[56] Since the easy axes of the nanocrystals are randomly oriented, the film behaves as a composite with no average magnetocrystalline anisotropy. As a result, the average remanent moment remains pointed in the direction of the external field that was last applied to saturate the individual moments. The average remanent moment can be manipulated to be in any direction, as shown in Fig. 6.3(d)-(f). After magnetizing the film to the right, the phase shift pattern of the average remanent state was inverted, as shown in Fig. 6.3(d). When the film was magnetized perpendicular to the surface, either upward or downward, the phase shift patterns also changed according to the magnetization direction as shown in Fig. 6.3(e) and (f). When the magnetization direction of the MFM tip was reversed to the upward direction, all the phase shift patterns in Figs. 6.3(c), (d), (e), and (f) were also inverted, as expected.

There is no evidence of any domain-wall structure, which is usually seen on continuous ferromagnetic materials, in Figs. 6.3(c), (d), (e), and (f), or any of our data. This suggests that the magnetic interactions between nanocrystals in the composite film are weak and that the single domains in the nanocrystals are more affected by the external field and by their individual magnetocrystalline anisotropy.

6.3 Micromagnetic model

To support this unusual model, we compared the approximate magnetic energies due to the external field, magnetocrystalline anisotropy, and dipole interaction, with details given in appendix A. The external field energy ($E_H = -\mathbf{m} \cdot \mathbf{H_{ex}}$) is 1.0×10^{-11} erg when the external field (H_{ex}) is 8 Tesla. We calculated the magnetic moment ($m=1.3\times10^{-16}$ emu) from the saturation magnetization of 1140 emu/cm^3[70] and a 6-nm-diameter FePt. The anisotropy energy ($E_{AN} = K\cdot V\sin^2\theta$) has a maximum value of $\sim7.9\times10^{-12}$ erg given the anisotropy constant (K) of 7×10^7 erg/cm^3.[61] The dipole interaction energy is given by $E_D = -\mu^2\ [3(\mathbf{m_1}\cdot\mathbf{r})(\mathbf{m_2}\cdot\mathbf{r}) - \mathbf{m_1}\cdot\mathbf{m_2}]/r^3$, where μ is the permeability of the medium surrounding the magnetic particles, and $\mathbf{m_1}$, $\mathbf{m_2}$ are the dipole moments of two interacting nanocrystals separated by the vector $\mathbf{r}$. This dipole interaction energy has a maximum value of 4.8×10^{-17} erg when $\mathbf{m_1}$, $\mathbf{m_2}$, and $\mathbf{r}$ are parallel, and $r = 40$ nm. Therefore the magnetic anisotropy energy dominates the dipole interaction in the remanent state. These calculations also confirm that an 8 Tesla external field can align the directions of these nanocrystal single domains.

From the X-ray, SQUID, MFM data we have developed a model where the FePt nanocrystals are randomly oriented and are almost non-interacting single domains in the remanent state. Figure 3 illustrates this simple model of how single domains behave in response to the external field. Figs. 6.4(a), (b), (c), and (d) describe the state at zero field after applying 8 Tesla to the left and to the right along the film plane, and in the up and down direction perpendicular to the film plane, respectively. In Fig. 6.4, the FePt cores in the nanocrystals have single domains with easy axes indicated by the red and blue arrows. The FePt nanocrystals with red arrows have their easy axes oriented with a significant component along the film plane, while nanocrystals with blue arrows have their easy axes closer to the perpendicular to the film plane. In this model, the red and blue arrows can only reverse direction after a strong field has been applied, since the magnetocrystalline energy is greater than the dipole interaction energy. When the 8 Tesla field is applied, it aligns all of the moments in the direction of the field. When the field is removed, the magnetization of each nanocrystal relaxes to its easy axis, but since it has two choices in the direction it will choose the direction that is closest to the applied field direction. In other words, all the nanocrystals will have a component of their remanent magnetization along the saturating field that was last applied, except for the few nanocrystals with easy axes exactly perpendicular to the saturating applied field. Therefore, the film retains an average remanent moment in the direction of the original saturating field because it is a composite with randomly oriented nanocrystals.

In Fig. 6.4(a), when the external field is applied to the left along the film plane, all the single domains align with their individual moments pointing to the left (not shown). After removing the external field, the film retains a net magnetic moment pointing to the left, as shown in Fig. 6.4(a), where the horizontal components of all the remanent moments point to the left. The dashed lines show the phase shift of the cantilever when the MFM tip is magnetized downward. If there is an attractive force between tip and sample, the phase shift is negative. A repulsive force gives a positive phase shift.[5][42] Fig. 6.4(a), (b), (c), and (d) are qualitative explanations for Figs. 6.3(c), (d), (e), and (f). We also simulated the case shown in Figs. 6.4(b) and (c) using a 150 × 200 × 50 array of magnetic dipoles, with results displayed in Fig. 6.5. The simulations show qualitatively the same patterns as the experimental results shown in Figs. 6.3(d) and (e). The details of the MFM profile simulation are described in appendix B.

6.4 Further confirmation

Thinner films with trenches were also studied. Fig. 6.6(a) shows the topography of a 900-nm-thick nanocrystal composite film. The MFM tip was magnetized downward. After magnetizing the film to the left with an 8 Tesla field, the film was scanned in the floating mode, 650 nm above the film surface. The result is shown in Fig. 6.6(b). Fig. 6.6(c) is the MFM image obtained using floating mode (with h = 630 nm) after applying the external field to the right along the film plane. Like Fig. 6.3(c) and (d), the phase shift was inverted in Fig. 6.6(b) and (c). We also made a 100-nm-thick film with trenches, as shown in Fig. 6.6(d). The film was magnetized to the left along the film plane and then scanned using floating mode (h = 490 nm) with a tip magnetized upward. The result is shown Fig. 6.6(e). Fig. 6.6(f) is an MFM image obtained in floating mode (h = 450nm) with a tip magnetized downward. In the case of the 100-nm-thick film, we averaged more lines than with the thicker films and used a high moment MFM tip (MESP-HM from Veeco, coated with CoCr) to increase the signal-to-noise ratio. Even though the MFM images are noisy, the inversion in the phase shift pattern was evident when the tip magnetization direction was reversed. Therefore, the behavior of the 100-nm-thick film is consistent with the thicker films and the model presented here.

6.5 Summary

In summary, 6-nm-diameter FePt nanocrystals were synthesized and coated with a ∼17-nm-thick silica shell. Annealing under hydrogen at 700°C for 30 min transformed the nanocrystals into the $L1_0$ ferromagnetic phase with a coercivity of 5 kOe at room temperature. From SQUID magnetometry and MFM studies, we conclude that the FePt nanocrystals in the remanent state behave as nearly non-interacting single domains. The silica coating prevents sintering of the magnetic nanocrystals and maintains a consistent average interparticle spacing in the composite that is large enough to nearly eliminate dipole coupling between neighboring particles. Furthermore, since $L1_0$ FePt has a high magnetocrystalline anisotropy, the composite film can be permanently magnetized at room temperature, even though the magnetic particle size is well below the characteristic magnetic domain size in bulk FePt. This is not possible with nanocrystals in the same size range made from softer magnetic materials like Co and Fe due to the superparamagnetic effect. When the external field direction was changed, the magnetization directions of the individual particles also changed direction. While these rather thick nanocrystal films are not useful for magnetic data storage, monolayer or few-layer films are an interesting possibility for such applications. Our study is one step towards understanding the micromagnetic properties of these nanocrystals. These single domain nanoparticles have advantages over continuous metal films used in current technology. First, FePt has high magnetocrystalline anisotropy, and second, the distance between two contiguous bits can be reduced to a nanoparticle diameter.

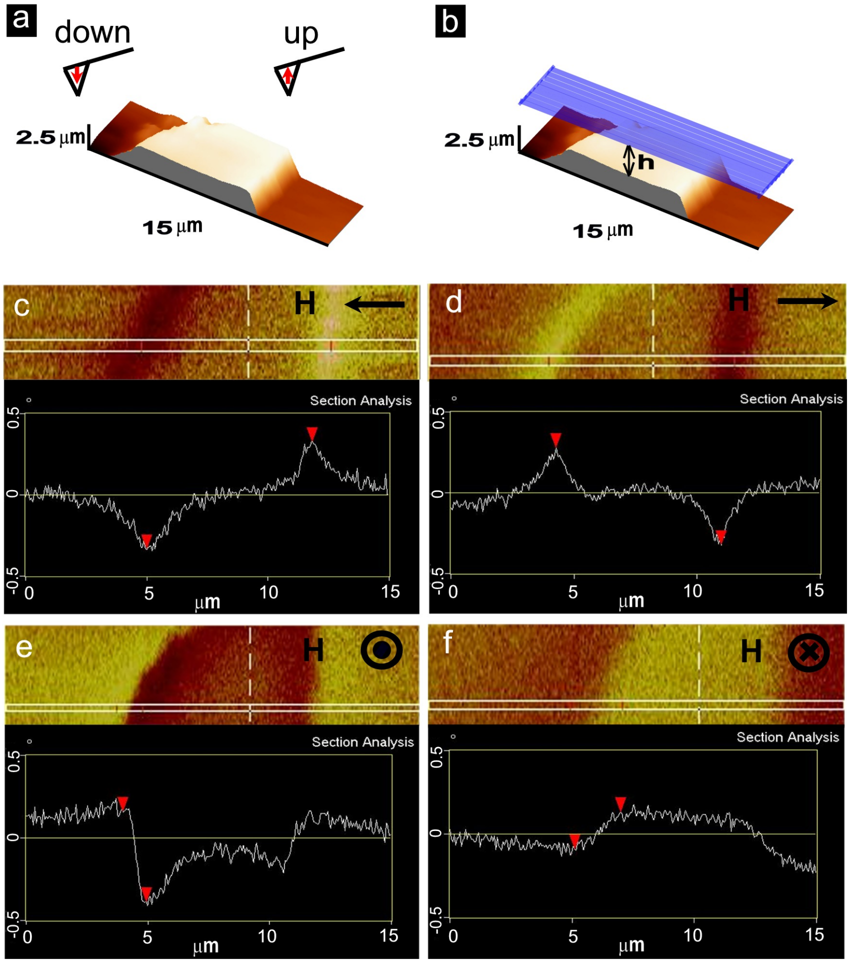

Figure 6.3: (a) Topography of a part of an island in a 2.5 μm-thick film. The tip can be magnetized upward or downward. (b) Schematic of the floating mode used to obtain the data, where h is the distance above the film surface. (c), (d), (e), and (f) show the phase shift of the oscillating cantilever in the floating mode, and the corresponding section analysis, obtained at zero field after applying 8 Tesla to the left and to the right along the film plane, and up and down in the direction perpendicular to the film plane, respectively. The line profile in the section analysis is the average between two horizontal white lines in the MFM image.

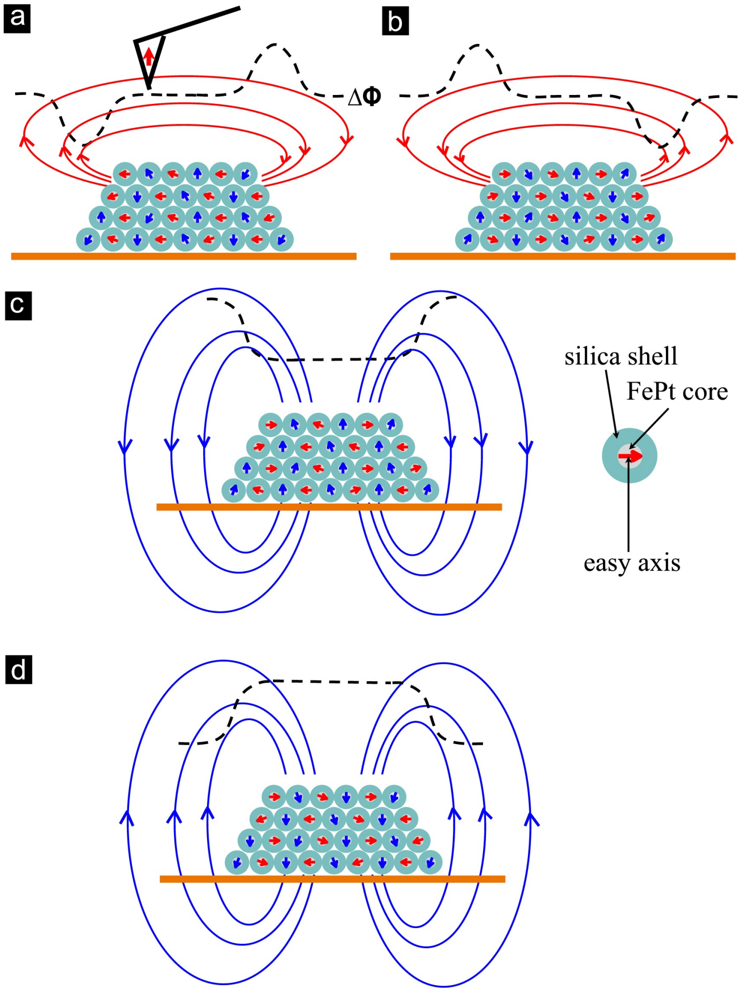

Figure 6.4: Model of single domain behavior in an external field. (a), (b), (c), and (d) illustrate remanent states after applying 8 T to the left and to the right along the film plane, and up and down in the direction perpendicular to the film plane, respectively. The FePt nanocrystals with red arrows have easy axis closer to the film plane and nanocrystals with blue arrows have easy axis closer to the perpendicular to the film plane. In this model, red and blue arrows cannot rotate in the remanent state, but can only flip, since the magnetocrystalline energy is greater than the dipole interaction energy. The black dashed lines show the phase shift of the cantilever when the MFM tip is magnetized downward.

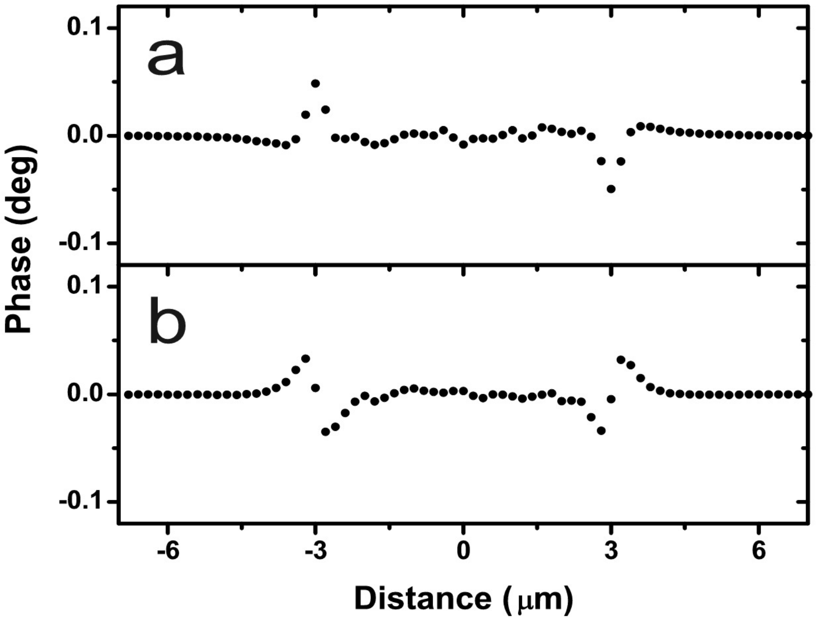

Figure 6.5: MFM phase shift as a function of distance calculated numerically using a 150 × 200 × 50 array of magnetic dipoles. In (a) the saturating field was applied to the left and in (b) in the upward direction, perpendicular to the film. The peaks and dips at 3 μm are in qualitative agreement with the expected profile in Figs. 6.4(b) and (c) and the experimental results in Figs. 6.3(d) and (e). The details of the MFM profile simulation are described in appendix B.

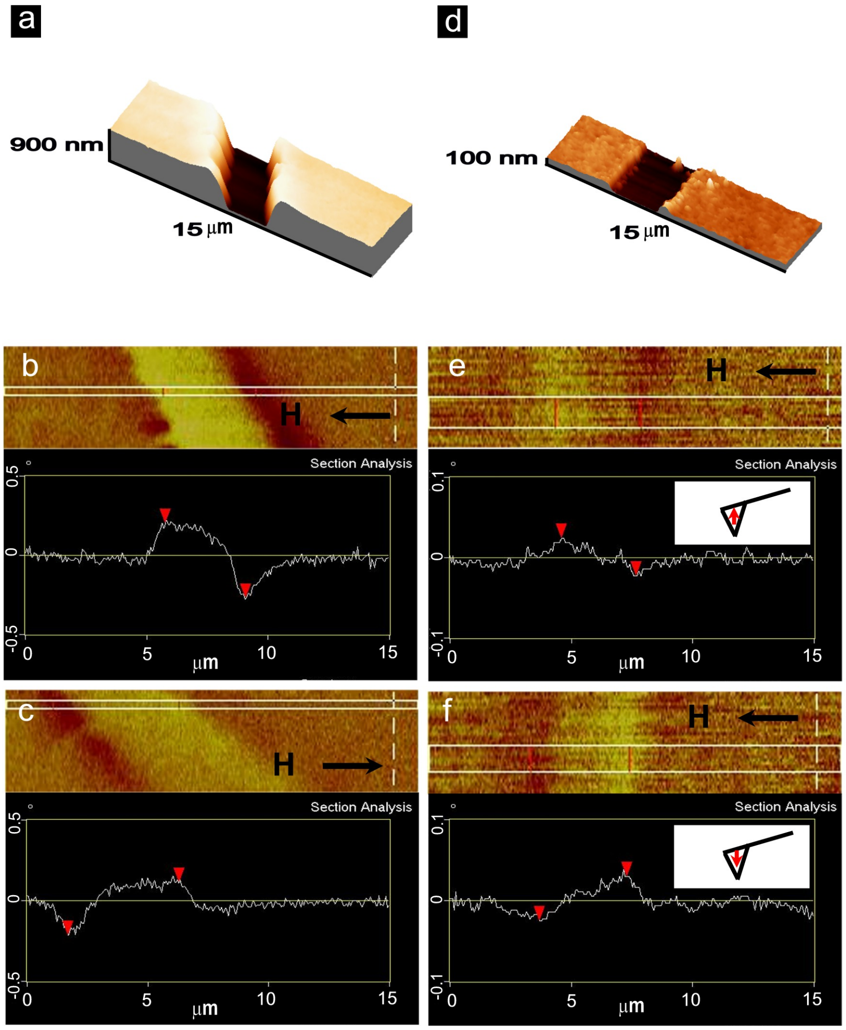

Figure 6.6: (a) Topography of a trench in a 900-nm-thick film composed of single domain nanocrystals. MFM image of the area shown in (a) obtained with a downward-magnetized MFM tip with the film in the remanent state after applying 8 T in the direction to the left (b) or to the right (c) along the film plane. (d) Topography of a trench in a 100-nm-thick film composed of single domain nanocrystals. MFM images of the remanent state of the area shown in (d) after applying 8 T in the direction to the left along the film plane, taken with an MFM tip magnetized upward (e) or downward (f).

Appendices

Appendix A

Magnetic Energies in a FePt Nanocrystal

For a FePt core with a diameter of 6 nm, using the saturation magnetization value of bulk FePt, namely 1140 emu/cc [45]:

m = 1140(emu/cc)$\times$(4π/3)$\times$(3$\times 10^{-7}$cm)^3 = 1.3 $\times 10^{-16}$ emu = 1.3 $\times 10^{-19}$ Am^2

For a silica sphere with a diameter of 39 nm at 5 Tesla:

m = 29.6 $\times 10^{-6}$ (emu/g Oe) $\times$(4π/3)$\times$(19.5$\times 10^{-7}$cm)^3 $\times$(2.6 g/cc)$\times$(50,000 Oe)= 1.2 $\times 10^{-20}$ emu

Therefore the silica shell has a negligible saturation magnetic moment.

Calculation of the external field energy (E$_H$) at 8 Tesla

From above, m = 1.3$\times 10^{-16}$ emu

E$_H$ = $-$m$\cdot$H$_{ex}$= (1.3$\times 10^{-16}$) $\times$(8$\times 10^4$) = 1.0$\times 10^{-11}$ erg

Calculation of the anisotropy energy (E$_{AN}$)

We used an anisotropy constant K = 7×10^{7} erg/cc [45] and $\theta = \pi/2$.

$\mathrm{E}_{AN} = \mathrm{K}\times\mathrm{V}\times\sin^2\theta = (7\times10^{7}\ \mathrm{erg/cc})\times(113\times10^{-21}\ \mathrm{cc}) = 7.9\ \times10^{-12}$ erg

Calculation of the dipole interaction energy ($\mathbf{E}_D$)

Mass susceptibility of silica = -29.6×10^{-6} emu/g Oe

Volume susceptibility $\chi = -29.6\times10^{-6}$ (emu/g Oe) × (density of silica) = $-29.6\times\ 10^{-6}$ (emu/g Oe)×(2g/cc) $\approx 5\times10^{-5}$ emu/cc, therefore $\mu = 1 + 4\pi\chi \approx 1$.

$\mathrm{E}_D = -\mu^2\ [3(\mathbf{m_1}\cdot\mathbf{r})(\mathbf{m_2}\cdot\mathbf{r}) - \mathbf{m_1}\cdot\mathbf{m_2}]/\mathrm{r}^3$

Maximum of $\mathrm{E}_D = \mu^2\ [2(\mathbf{m_1}\cdot\mathbf{m_1})]/\mathrm{r}^3 = 2\times\ (1.3\times10^{-16}\mathrm{emu})\ \times(1.3\times10^{-16}\ \mathrm{emu})/\ (39\mathrm{nm})^3 = 2\times(1.69\times10^{-32})\ /\ (5.9\times10^{-17}\ \mathrm{cc}) = 5.7\times10^{-17}$ erg

Appendix B

Simulation of the MFM Profile

We simulate the MFM signal from a FePt nanocrystal composite film. Our model is a 150 × 200 × 50 array of magnetic dipoles with dimensions of 6μm × 8μm × 1μm. The unit cell of the array is 40nm$\hat{x}$ + 40nm$\hat{y}$ − 20nm$\hat{z}$. The FePt point dipoles are located at each lattice point with random directions of their uniaxial anisotropy. The total stray field **B** from the film will be the sum of the fields produced by each point dipole $\mathbf{m}_{ijk}$

$$\mathbf{B} = \frac{\mu_0}{4\pi}\sum_{i,j,k}\left(\frac{3[\mathbf{m_{ijk}}\cdot(\mathbf{r}-\mathbf{r_{ijk}})](\mathbf{r}-\mathbf{r_{ijk}})}{|\mathbf{r}-\mathbf{r_{ijk}}|^5} - \frac{\mathbf{m_{ijk}}}{|\mathbf{r}-\mathbf{r_{ijk}}|^3}\right) \qquad \text{(B.1)}$$

where μ_0 is the permeability of vacuum, $\mathbf{r} = \mathrm{x}\hat{x} + \mathrm{y}\hat{y} + \mathrm{z}\hat{z}$ is the position where the field is evaluated, $\mathbf{r}_{ijk}$= (3μm +i·40nm)$\hat{x}$ + j·40nm$\hat{y}$ − k·20nm$\hat{z}$ and $\mathbf{m}_{ijk}$= $\mathrm{M}_{FePt}(\alpha_{ijk}\hat{x} + \beta_{ijk}\hat{y} + \gamma_{ijk}\hat{z})$, where i, j, k are integers (1≤i≤150, 1≤j≤200, 1≤k≤50). M_{FePt} is the amplitude of magnetic moment for a 6 nm-size FePt nanocrystal and α_{ijk}, β_{ijk} and γ_{ijk} are the direction cosines of the magnetic moment $\mathbf{m}_{ijk}$ with respect to x, y, z axes.

We consider the MFM tip as a point dipole moment. The direction of the MFM tip is approximately along the z axis, so the phase shift $\Delta\phi$ can be expressed as [34]

$$\Delta\phi = -\frac{Q}{k}\left(\frac{\partial F}{\partial z}\right) = m_{ijk}\frac{Q}{k}\frac{\partial^2(\mathbf{B}\cdot\hat{z})}{\partial^2 z} \tag{B.2}$$

where Q and k are the quality factor and spring constant of the cantilever, respectively, F is magnetic force that the film exerts on the tip, and m$_{tip}$ is the magnitude of the tip moment.

The α_{ijk}, β_{ijk} and γ_{ijk} are generated by a random number generator and then normalized. We take the absolute value of α_{ijk} to simulate a remanent state after applying 8 Tesla field along the positive x direction. We set the 'floating height' as 400nm, so $\mathbf{r}$ will trace the line between $-7\mu\text{m}\hat{x} + 4\mu\text{m}\hat{y} + 0.4\mu\text{m}\hat{z}$ and $7\mu\text{m}\hat{x} + 4\mu\text{m}\hat{y} + 0.4\mu\text{m}\hat{z}$, as shown in Fig. B.1. We first calculate the z component of $\mathbf{B}$, namely B_z , at $z_0 = 400$nm, $z_1 = 400$nm $-$ Δz and $z_2 = 400$nm $-$ 2Δz. Then the second derivative of B_z with respect z can be calculated by

We set the effective MFM tip's moment (m$_{tip}$) as 3.7×10^{-15} Am^2, as in ref.[60], although this only changes the magnitude of the result and not the patterns obtained. Typical values of Q and k are used[34] (200 and 2N/m, respectively) and $M_{FePt} = 1.3\times10^{-15}$ Am^2 was estimated from the nanocrystal size and the magnetic moment of bulk FePt.

The simulated MFM phase shift profiles shown in Fig. B.2(a) and (b) are qualitatively the same as the experimental results in Figs. 6.4(d) and (e) in the manuscript. The fluctuations in the MFM phase profile between the ends of the film are probably due to the finite size of the simulation. This is supported by running the program with a different set of random numbers, which changes these fluctuations but leaves unchanged the important peak/dip structures at the ends of the film. The overall magnitude of the phase shift is smaller than the experimental value, but this is reasonable given that the simulation is for a thinner film (1.0 μm vs. 2.5 μm for the experiment) and the uncertainty in some parameters such as k or the tip's moment.

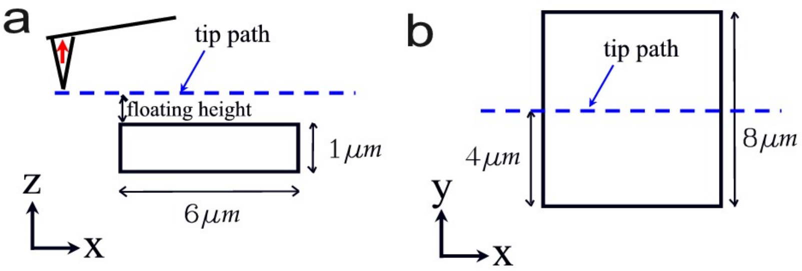

Figure B.1: (a) Side view of the path followed by the MFM tip. The tip is magnetized upward. (b) Top view of the MFM tip path. A point dipole is located at each 40nm × 40nm × 20nm cell in the 6 μm × 8 μm × 1 μm size film.

Fig. B.3 shows that the important features, namely the peaks and dips at the edge of the film, are insensitive to details of the model such as the random sequence used, the choice of body centered or rectangular structure for the packing of the nanocrystals, or using random cosine angles or random angles for their orientations. The smaller peaks and dips above the middle of the film do depend on these details. The most likely explanation for this sensitivity is that the MFM tip was modeled as a point dipole, which has infinite spatial resolution. The actual MFM tip is a spatially distributed single dipole at best, or a superposition of such dipoles.

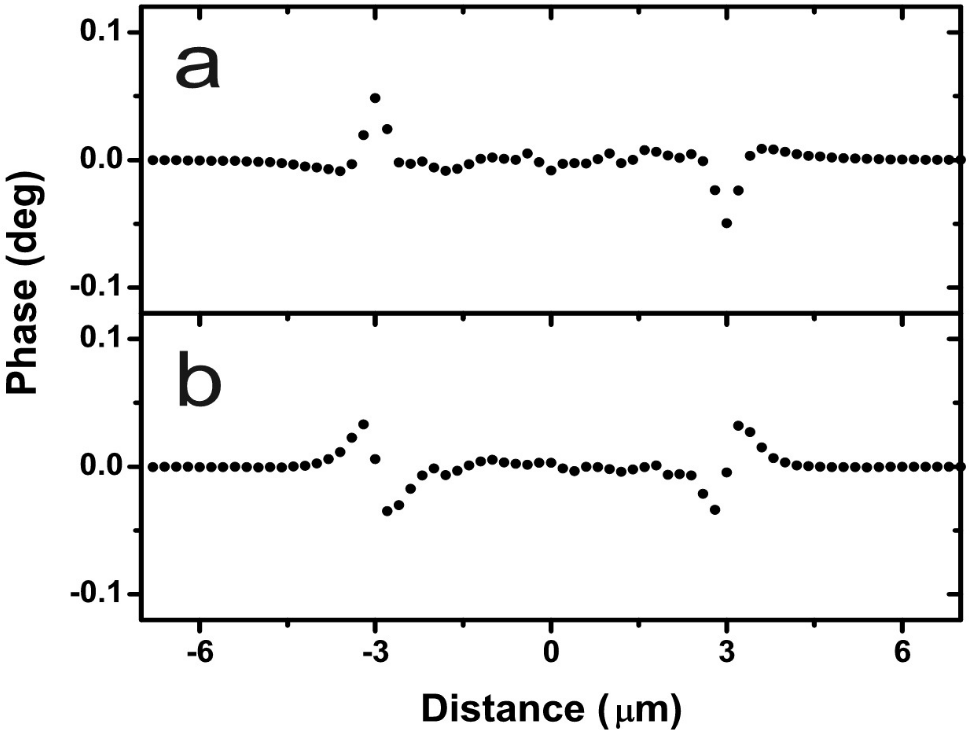

Figure B.2: MFM phase shift as a function of distance calculated numerically using a 150 × 200 × 50 array of magnetic dipoles. In (a) the saturating field was applied to the left and in (b) in the upward direction, perpendicular to the film. The peaks and dips at 3 μm are in qualitative agreement with the expected profile in Figs. 6.4(b) and (c) and the experimental results in Figs. 6.3(d) and (e).

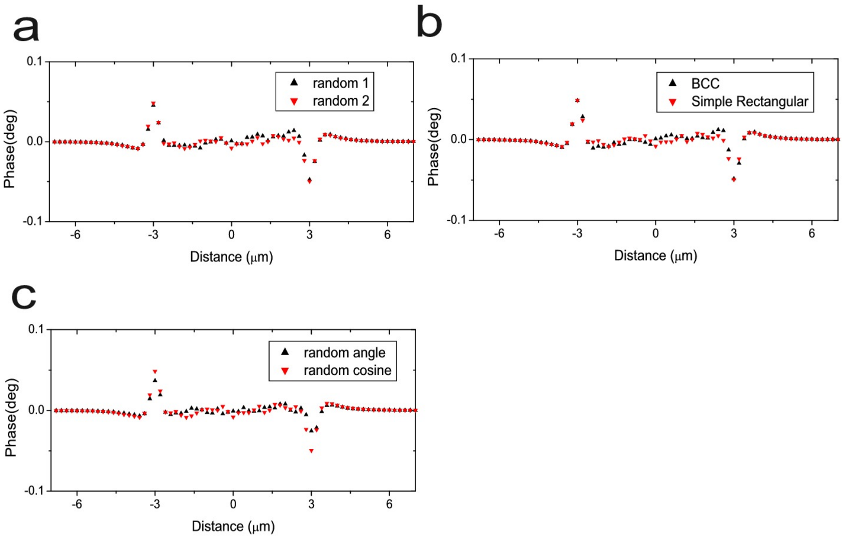

Figure B.3: Comparison of one-dimensional MFM phase shift simulations resulting from the remanent state of an island film after applying 8 Tesla field in the positive x direction with the conditions of (a) different random sequences for determining the orientations of the nanocrystal domains, (b) body centered cubic and simple rectangular structure, and (c) random angle and random cosine generators. The tip line path and the island film model are shown in Fig. B.1.

Appendix C

Resistance measurement of FePt nanocrystals

In chapter 6, we studied the 6-nm size FePt nanocrystals and showed that the FePt nanocrystal can be a ferromagnet with high coercivity at room temperature. Therefore, spin-dependent tunneling in nanocrystals can be a good study topic for FePt nanocrystals. Black et. al already studied spin-dependent tunneling through Cobalt-Nanocrystals.[74] They made lithographically patterned tunnel-junction in Fig. C.1(a). Then they deposited a few layers of 10 nm size Cobalt nanocrystals and annealed them at 400°C to reduce the space between nanocrystals by burning the stabilizer coating. They showed that the magnetoresistance changes due to changes in the nanocrystal magnetic moment, as shown in Fig. C.1(b).

C.1 Device Fabrication

The patterned tunnel-junction arrays are fabricated by e-beam lithography technique. The lithography device is composed of four steps as shown in Fig. C.2: (a) Polymethyl methacrylate (PMMA) resist coating and e-beam exposure, (b) development, (c) metal deposition, and (d) lift-off.

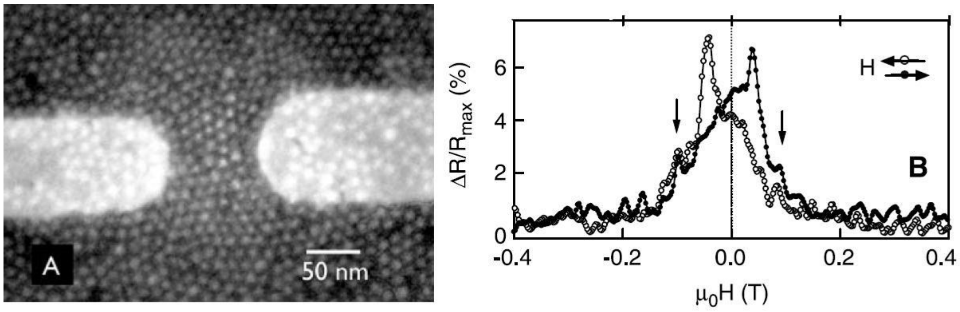

Figure C.1: (a) SEM image of self-assembled Co-nanocrystal superlattice device (from Ref. [74]) (b) Magnetoresistance of Co-nanocrystal device at 2K (from Ref. [74]).

C.1.1 PMMA resist coating and e-beam exposure

Bi-layer of PMMA coating is used to shape an undercut in development step. To make the first layer, 4.7 g of 38,000 molecular weight PMMA (Across Organics) is dissolved in 50 ml chlorobenzene (99%, Across Organics) and then stirred for more than 24 hours with a stirrer bar. The PMMA solution is dropped on a Silicon on insulator (SOI) wafer film, then spun at 6000 RPM for 60 seconds. The film is baked in an oven at 170°C for 30 minutes. The second layer is coated in a similar way, except that 4.7 g of 996,000 molecular weight PMMA (Aldrich) is dissolved in 100 ml chlorobenzene. The pattern in Figs. C.3(a) and (b) is designed with a pattern editor in a Raith 50 system. The junction gap size is designed as 150 nm. The bi-layer PMMA film is exposed to a 20 keV electron beam using the Raith 50. The area dose is about 215 μC/cm^2.

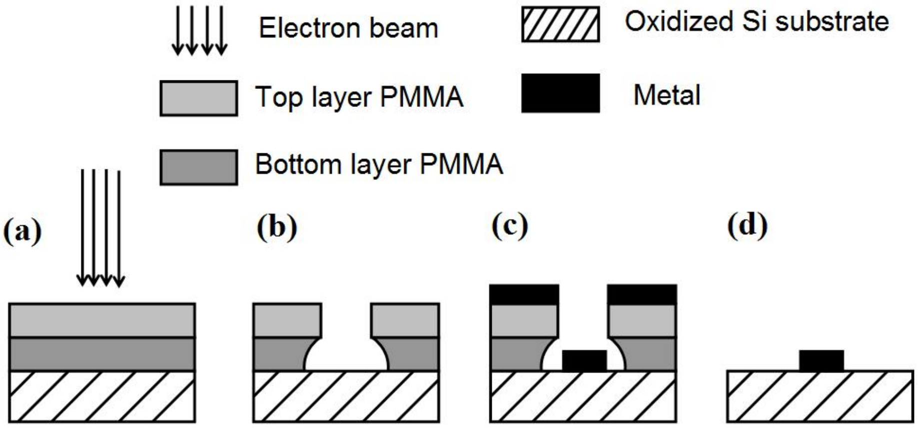

Figure C.2: Electron beam lithography process. (a) PMMA coating and e-beam exposure. (b) development. (c) metal deposition. (d) lift-off.

C.1.2 Development

The e-beam exposed PMMA is dissolved for 60 seconds in a developer, which is 1:3 mixture of methyl-isobutyl-ketone (MIBK) and Isopropyl alcohol (IPA). Sometimes 60 seconds development causes overdevelopment in some patterns, so the developing time needs to be reduced to 30 seconds. After developing, the film is rinsed in IPA for 60 seconds.

C.1.3 Metal Deposition

Thermal evaporation and sputtering are used to deposit metal on the developed film. For the alloy deposition, such as AuPt, sputtering is used. Mostly Au is deposited and thermal evaporation is used for the Au deposition as shown in Fig. C.3(c).

C.1.4 Lift-off

After the metal deposition, the PMMA mask is removed in boiling acetone. The film is soaked in a beaker filled with acetone and the beaker is indirectly heated in a water-filled flask. The film is soaked for 7 minutes then gently shaken for 5 minutes. To remove the PMMA residue completely, the same procedure will be repeated three times. Then the film is rinsed in boiling IPA. In case of Au coating, the bonding force on a SOI wafer is weak, so sonication or pipette blowing should be avoided.

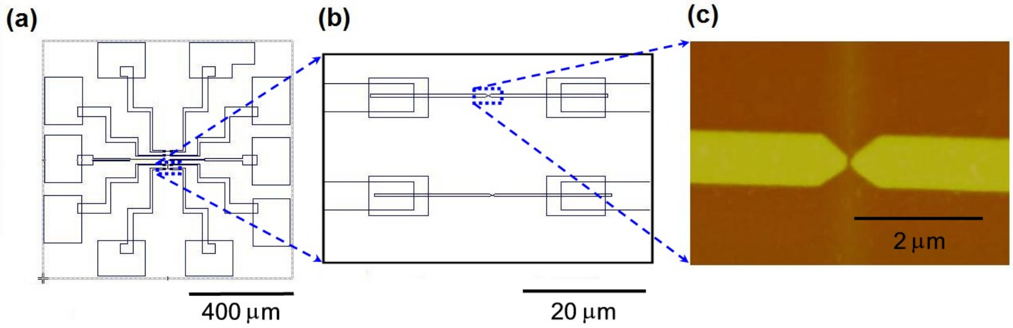

Figure C.3: (a) and (b) Schematic diagram of e-beam exposure area generated by Raith 50. (c) AFM image of after lift-off.

C.2 Sample Preparation

The 6nm size FePt nanocrystals are synthesized as explained in chapter 6, then drop-casted onto AuPt tunnel junction arrays. Then the sample is annealed in a quartz tube furnace with a forming gas (93% N_2/ 7% H_2) at different temperatures for 30 minutes.

C.3 Resistance Measurement of FePt Nanocrystals

After annealing, the sample is attached on a 28-pin chip carrier (Spectrum, LCC02834). Then each metal tunnel junction on the SOI wafer is connected to an Au-plated pad on the chip carrier with an Al bonding wire using an ultrasonic bonder (West Bond, 7476D). As shown in Fig. C.4, the applied voltage is usually ramped from -100mV to 100mV using data acquisition card (National Instruments, NIDAQ 831) across nanocrystals. The tunneling current is amplified by a current amplifier (Keithley, 428 current amplifier). The amplified signal is then read by the ADC of the data acquisition card. All the output and input voltages are recorded by a LabVIEW program.

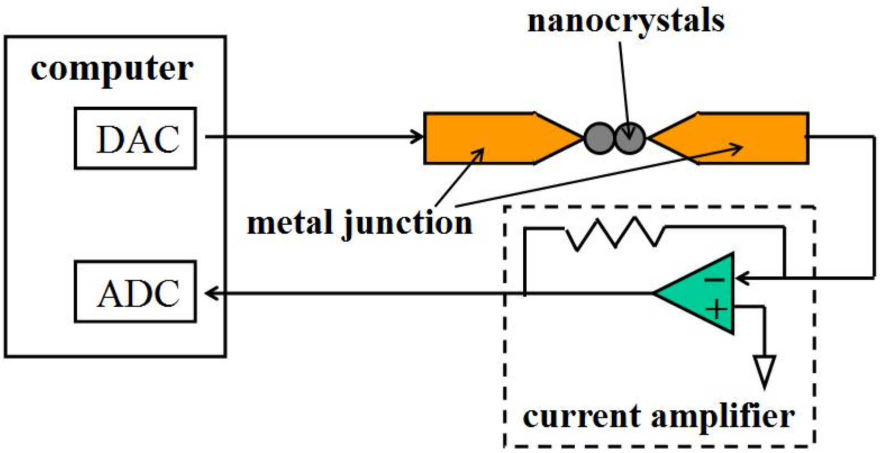

Figure C.4: Schematic diagram of measurement setup.

C.4 Summary

It was hard to control the stabilizer length with the annealing process. The measured resistances were either infinite or a few hundred ohms. So we tried ligand exchange to reduce the spacing between nanocrystals.[75] The Fig. C.5(a) is a TEM image, obtained with original FePt nanocrystals. The Fig. C.5(b) is a TEM image, taken after ligand exchange with octane thiol. Even after ligand exchange, the measured resistance is about 10∼25 GΩ. These values are still big since we need to measure a resistance around 4 K. If we do not anneal the FePt Nanocrystals, the Curie temperature is about 20 K. The resistance will increase by one order if we lower the temperature to 4 K. Therefore we need to find another way to increase the resistance of FePt nanocrystals in-between tunnel junctions.

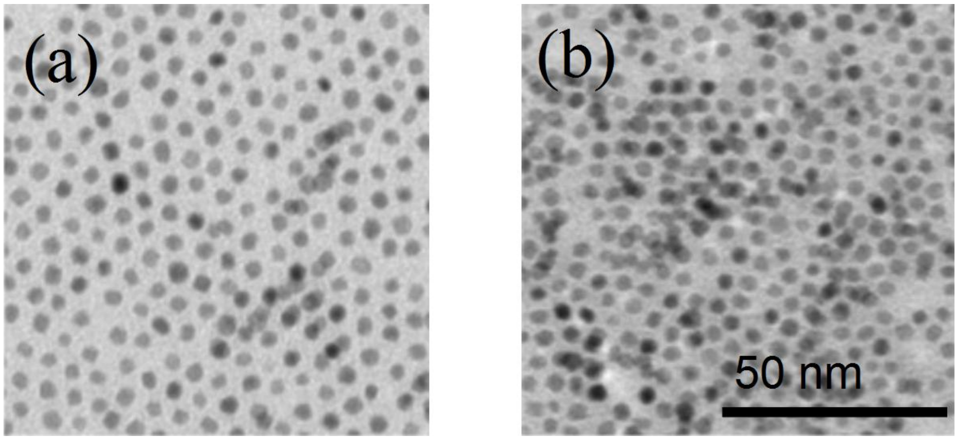

Figure C.5: TEM images of 6nm size FePt nanocrystals with oleylamine and oleic acid ligand (a) and with octanethiol (b).

Bibliography

[1] G. Binnig, H. Rohrer, Ch. Gerber, and E. Weibel. *Phys. Rev. Lett.*, 49:57, 1982.

[2] G. Binnig, C. F. Quate, , and Ch. Gerber. *Phys. Rev. Lett.*, 56:930, 1982.

[3] Y. Martin and H. K. Wickramasinghe. *Appl. Phys. Lett.*, 50:1455, 1987.

[4] Y. Martin, D. W. Abraham, and H. K. Wickramasinghe. *Appl. Phys. Lett.*, 52:1103, 1988.

[5] D. Rugar, H. J. Mamin, P. Guethner, S. E. Lambert, J. E. Stern, I. McFadyen, and T. Yogi. *J. Appl. Phys.*, 68:1169, 1990.

[6] A. Wadas and H. J. Hug. *J. Appl. Phys.*, 72:203, 1992.

[7] H. J. Hug, B. Stiefel, P. J. A. van Schendel, A. Moser, R. Hofer, S. Martin, H.-J. Güntherodt, S. Porthun, L. Abelmann, J. C. Lodder, G. Bochi, and R. C. O'Handley. *J. Appl. Phys.*, 83:5609, 1998.

[8] Y. Martin, C. C. Williams, and H. K. Wickramasinghe. *J. Appl. Phys.*, 61:4723, 1987.

[9] T. R. Albrecht, P. Grütter, D. Horne, and D. Rugar. *J. Appl. Phys.*, 69:668, 1991.

[10] U. H. Pi, Z. G. Khim, D. H. Kim, A. Schwarz, M. Liebmann, and R. Wiesendanger. *Phys. Rev. B*, 73:144505, 2006.

[11] M. Roseman and P. Grütter. *J. Appl. Phys.*, 91:8840, 2002.

[12] A. Volodin, K. Temst, C. Van Haesendonck, and Y. Bruynseraede. *Rev. Sci. Instrum.*, 71:4468, 2000.

[13] C. Israel, C. Hyun, A. de Lozanne, S. Phark, and Z. G. Khim. *Rev. Sci. Instrum.*, 77:23704, 2006.

[14] T. Chuang and A. de Lozanne. *Rev. Sci. Instrum.*, 78:53710, 2007.

[15] M. Tortonese, R. C. Barrett, and C. F. Quate. *Appl. Phys. Lett.*, 62:834, 1993.

[16] F. J. Giessibl and B. M. Trafas. *Rev. Sci. Instrum.*, 65:1923, 1994.

[17] L. A. Giannuzzi and F. A. Stevie. *Introduction to Focused Ion Beams: Instrumentation, Theory, Techniques and Practice.* Springer, New York, 2005.

[18] J. Orloff, M. Utlaut, and L. Swanson. *High Resolution Focused Ion Beams: FIB and its applications.* Springer, 2002.

[19] F. Watt, A. A. Bettiol, J. A. van Kan, E. J. Teo, and M. B. H. Breese. *International Journal of Nanoscience*, 4:269, 2005.

[20] P. Grütter, D. Ruger, H. J. Mamin, G. Castillo, S. E. Lambert, C-J. Lin, R. M. Valletta, O. Wolter, T. Bayer, and J. Greschner. *Appl. Phys. Lett.*, 57:1820, 1998.

[21] Y. Wu, Y. Shen, Z. Liu, K. Li, and J. Qiu. *Appl. Phys. Lett.*, 82:1748, 2003.

[22] C. W. Yuan, Z. Zheng, A. L. de Lozanne, M. Tortonese, D. A. Rudman, and J. N. Eckstein. *J. Vac. Sci. Technol. B*, 14:1210, 1996.

[23] B. Ilic, H. G. Craighead, S. Krylov, W. Senaratne, C. Ober, and P. Neuzil. *J. Appl. Phys.*, 95:3694, 2004.

[24] K. L. Ekinch, Y. T. Yang, and M. L. Roukes. *J. Appl. Phys.*, 95:2682, 2004.

[25] T. D. Lee, M. S. Hwang, and K. J. Lee. *J. Magn. Magn. Mat.*, 235:297, 2001.

[26] U. Hartmann. *Annu. Rev. Mater. Sci.*, 29:53, 1999.

[27] M. S. Valera and A. N. Farley. *Meas. Sci. Technol.*, 7:30, 1996.

[28] Z. Liu, Y. Dan, Q. Jinjun, and Y. Wu. *J. Appl. Phys.*, 91:8843, 2002.

[29] D. Litvinov adn S Khizroev. *Appl. Phys. Lett.*, 81:1878, 2002.

[30] L. Gao, L. P. Yue, T. Yokota, R. Skomski, S. H. Liou, H. Takahoshi, H. Saito, and S. Ishio. *IEEE Trans. Magn.*, 40:2194, 2004.

[31] Z. Deng, E. Yenilmez, J. Leu, J. E. Hoffman, E. W. J. Straver, H. Dai, and K. A. Moler. *Appl. Phys. Lett.*, 85:6263, 2004.

[32] H. Kuramochi, T. Uzumaki, M. Yasutake, A. Tanaka, H. Akinaga, and H. Yokoyama. *Nanotechnology*, 16:24, 2005.

[33] P. J. A. van Schendel, H. J. Hug, B. Stiefel, S. Martin, and H.-J. Guntherodt. *J. Appl. Phys.*, 88:435, 2000.

[34] T. Kebe and A. Carl. *J. Appl. Phys.*, 95:775, 2004.

[35] R. Von Hemmont, J. Wecker, B. Holzapfel, L. Schultz, and K. Samwer. *Phys. Rev. Lett.*, 71:2331, 1993.

[36] S. Jin, T. H. Tiefel, M. McCormack, R. A. Fastnacht, R. Ramesh, and L. H. Chen. *Science*, 264:413, 1994.

[37] N. D. Mathur, G. Burnell, S. P. Isaac, T. J. Jackson, B.-S. Teo, J. L. MacManus-Driscoll, L. F. Cohen, J. E. Evetts, and M. G. Blamire. *Nature*, 387:266, 1997.

[38] K. Steenbeck, T. Eick, K. Kirsch, K. O'Donnell, and E. Steinbei. *Appl. Phys. Lett.*, 71:968, 1996.

[39] J. O'Donnell, M. S. Rzchowski, J. N. Eckstein, and I. Bozovic. *Appl. Phys. Lett.*, 72:1775, 1998.

[40] A. J. Millis. *Nature*, 392:147, 1998.

[41] C. Hyun, A. Lee, and A. deLozanne. *Nanotechnology*, 17:921, 2006.

[42] R. D. Gomez, A. O. Pak, A. J. Anderson, E. R. Burke, A. J. Leyendecker, and I. D. Mayergoyz. *J. Appl. Phys.*, 83:6226, 1998.

[43] C. Ruster, T. Borzenko, C. Gould, G. Schmidt, L. W. Molenkamp, X. Liu, T. J. Wojtowicz, J. K. Furdyna, Z. G. Yu, and M. E. Flatte. *Phys. Rev. Lett.*, 91:216602, 2003.

[44] Y. Lu, X. W. Li, G. Q. Gong, G. Xiao, A. Gupta, P. Lecoeur, J. Z. Sun, Y. Y. Wang, and V. P. Dravid. *Phys. Rev. B*, 54, 1996.

[45] D. Weller and A. Moser. *IEEE Trans. Magn.*, 35:4423, 1999.

[46] S. Sun, C. B. Murray, D. Weller, L. Folks, and A. Moser. *Science*, 287:1989, 2000.

[47] Z. R. Dai, S. Sun, and Z. L. Wang. *Nano Lett.*, 1:443, 2001.

[48] M. Tanase, N. T. Nuhfer, D. E. Laughlin, T. J. Klemmer, C. Liu, N. Shukla, X. Wu, and D. Weller. *J. Magn. Magn. Mat.*, 266:215, 2003.

[49] Y. Sasaki, M. Mizuno, A. C.C. Yu, M. Inoue, K. Yazawa, I. Ohta, M. Takahashi, B. Jeyadevan, and K. Tohji. *J. Magn. Magn. Mat.*, 282:122, 2004.

[50] T. J. Klemmer, C. Liu, N. Shukla, X. W. Wu, D. Weller, M. Tanase, D. E. Laughlin, and W. A. Soffa. *J. Magn. Magn. Mat.*, 266:79, 2003.

[51] C. Liu, X. Wu, T. Klemmer, N. Shukla, and D. Weller. *Chem. Mater.*, 17:620, 2005.

[52] U. Hartmann. *Annu. Rev. Mater.*, 29:53, 1999.

[53] V. F. Puntes, P. Gorostiza, D. M. Aruguete, N. G. Bastus, and A. P. Alibisatos. *Nature Mater.*, 3:263, 2004.

[54] S. A. Koch, R. H. te Velde, G. Palasantzas, and J. T. M. De Hosson. *Appl. Phys. Lett.*, 84:556, 2004.

[55] S. Ishio, G. Q. Li, H. Takahoshi, H. Ito, H. Saito, T. Shima, and K. Takanashi. *J. Magn. Magn. Mat.*, 272.

[56] T. Shima, K. Takanashi, Y. K. Takanashi, K. Hono, G. Q. Li, and S. Ishio. *J. Magn. Magn. Mat.*, 266:171, 2003.

[57] G. Q. Li, H. Takahoshi, H. Ito, H. Saito, S. Ishio, T. Shima, and K. Takanashi. *J. Magn. Magn. Mat.*, 94:5612, 2003.

[58] S. Sun, S. Anders, H. f. Hamann, J-U. Thiele, J. E. E. Baglin, T. Thomson, E. E. Fullerton, C. B. Murray, and B. D. Terris. *J. Am. Chem. Soc.*, 124:2884, 2002.

[59] S. Sun, E. E. Fullerton, D. Weller, and C. B. Murray. *IEEE Trans. Magn.*, 37:1239, 2001.

[60] S. McVitie, R. P. Ferrier, J. Scott, G. S. White, , and A. J. Gallagher. *J. Appl. Phys.*, 89:3656, 2001.

[61] B. D. Cullity. *Elements of X-ray Diffraction.* Addison Wesley, 1892.

[62] G. A. Held, H. Zeng, and S. Sun. *J. Appl. Phys.*, 95:1481, 2004.

[63] S. Yamamoto, Y. Morimoto, T. Ono, and M. Takano. *Appl. Phys. Lett.*, 87:32503, 2005.

[64] D. C. Lee, F. V. Mikulec, J. M. Pelaez, K. Bonil, and B.A. Korgel. *J. Phys. Chem. B*, 110:11160, 2006.

[65] M. Chen, J. P. Liu, and S. Sun. *J. Am. Chem. Soc.*, 126:8394, 2004.

[66] H. Fan, K. Yang, D. M. Boye, and T. Sigmon. *Science*, 304:567, 2004.

[67] Z.W. Wilchinsky. *J. Appl. Phys.*, 15:806, 1944.

[68] J.A. Christodoulides, P. Farber, M. Danii, H. Okumura, G. C. Hadjipanayis, V. Skumryev, A. Simopoulos, and D. Weller. *J. Appl. Phys.*, 37:1292, 2001.

[69] E. C. Stoner and E. P. Wohlfarth. *Phil. Trans. R. Soc. A*, 240:599, 1948.

[70] R. C. Weast. *Handbook of Chemistry and Physics.* CRC Press, 55th edition, 1974.

[71] J-P. Wang, J-M. Qiu, T. A. Taton, and B-S. Kim. *IEEE Trans. Magn.*, 42:3042, 2006.

[72] B. A. Jones, J. D. Dutson, K. O'Grady, B. J. Hickey, D. Li, N. Poudyal, and J. P. Liu. *IEEE Trans. Magn.*, 42:3066, 2006.

[73] H. S. Nalwa. *Magnetic nanostructures.* American Scientific Publishers, 2002.

[74] C. T. Black, C. B. Murray, R. L. Sandstrom, and S. Sun. *Science*, 290:1131, 2000.

[75] H. G. Bagaria, E. T. Ada, M. Shamsuzzoha, D. E. Nikles, and D. T. Johnson. *Langmuir*, 22:7732, 2006.

Vita

Changbae Hyun was born in Shihung, Cheju, Republic of Korea on March 2, 1974, son of Doo-Chu Hyun and Chun-Ja Kang. In 1998 he received the Bachelor of Science in Physics from Seoul National University in Republic of Korea in 1998. After working for three years to fulfill mandatory military requirement, he entered the Graduate School at the University of Texas at Austin in 2002. He is expected to finish his graduate studies in 2007 after spending five years under the supervision of Prof. Alex de Lozanne.

Permanent address: 415W 39TH ST APT 104
Austin, Texas 78751

This dissertation was typeset with LaTeX[†] by the author.

[†] LaTeX is a document preparation system developed by Leslie Lamport as a special version of Donald Knuth's TeX Program.